Nonmuscle myosin IIB is a driver of cellular reprogramming

Amanda E. Balaban[a], Ly T. S. Nguyen[a], Eleana Parajón[a], and Douglas N. Robinson[a,b,c,*]
[a]Department of Cell Biology and [b]Departments of Pharmacology and Molecular Sciences, Medicine, and Oncology, Johns Hopkins University School of Medicine, Baltimore, MD 21205; [c]Chemical and Biomolecular Engineering, Johns Hopkins University, Baltimore, MD 21218

ABSTRACT **Nonmuscle myosin IIB (NMIIB) is considered a primary force generator during cell motility. Yet many cell types, including motile cells, do not necessarily express NMIIB. Given the potential of cell engineering for the next wave of technologies, adding back NMIIB could be a strategy for creating supercells with strategically altered cell morphology and motility. However, we wondered what unforeseen consequences could arise from such an approach. Here, we leveraged pancreatic cancer cells, which do not express NMIIB. We generated a series of cells where we added back NMIIB and strategic mutants that increase the ADP-bound time or alter the phosphorylation control of bipolar filament assembly. We characterized the cellular phenotypes and conducted RNA-seq analysis. The addition of NMIIB and the different mutants all have specific consequences for cell morphology, metabolism, cortical tension, mechanoresponsiveness, and gene expression. Major modes of ATP production are shifted, including alterations in spare respiratory capacity and the dependence on glycolysis or oxidative phosphorylation. Several metabolic and growth pathways undergo significant changes in gene expression. This work demonstrates that NMIIB is highly integrated with many cellular systems and simple cell engineering has a profound impact that extends beyond the primary contractile activity presumably being added to the cells.**

Monitoring Editor
Alex Dunn
Stanford University

Received: Aug 9, 2021
Revised: Mar 27, 2023
Accepted: Apr 10, 2023

INTRODUCTION

Nonmuscle myosin II (NMII) proteins play an integral role in cell shape control, including during processes like cytokinesis, cell motility, and tissue formation. As contractile proteins that generate mechanical forces to help guide the resistance and reshaping of cells, NMIIs are often deemed as residing at the bottom of signaling pathways that are triggered to initiate these cell behaviors. These signaling pathways lead to activation of Rho/ROCK, which trigger myosin light chain phosphorylation (Shutova and Svitkina, 2018). This light chain phosphorylation then places myosin II in an active state, promoting its assembly into bipolar filaments and/or stimulating motor activity, allowing the motor to engage with actin filaments to generate pulling forces. The mammalian genome encodes three NMIIs, including NMIIA, NMIIB, and NMIIC. NMIIA is a low processivity myosin, while NMIIB displays high processivity due to a longer ADP-bound lifetime (Norstrom *et al.*, 2010; Melli *et al.*, 2018). For processes such as cell motility of polarized cells, NMIIA generally resides toward the front of the cell, where it helps to tune the mechanical forces experienced by focal adhesion networks, while NMIIB resides over the nucleus and toward the rear of the cell, where it helps to generate mechanical stresses that help propel the cell forward (Shutova and Svitkina, 2018). NMIIC has a less-well-defined role as it is less abundantly expressed in mammalian cell types, but it does reside toward the front of a crawling cell and is associated with stress fibers in a manner similar to that of NMIIA (Surcel *et al.*, 2019).

Yet, despite this generalized description of the NMIIs, increasing evidence highlights their distinct roles. NMIIC, for example, is significantly less abundant than NMIIA or NMIIB (when IIB is present), yet it can have just as powerful an impact on cell mechanics as removal of the much more abundant NMIIA (Surcel *et al.*, 2019). Furthermore, while NMIIB is generally assigned the role of generating

This article was published online ahead of print in MBoC in Press (http://www.molbiolcell.org/cgi/doi/10.1091/mbc.E21-08-0386) on April 19, 2023.

Conflict of interest disclosure: D. N. Robinson is exploring a biotech startup company.

*Address correspondence to: Douglas N. Robinson (dnr@jhmi.edu).

Abbreviations used: ctr, control; FOV, field of view; IIB, NMIIB; NMII, nonmuscle myosin II; OxPhos, oxidative phosphorylation; ROI, region of interest.

contractile stresses that help propel the cell forward, many highly motile cells such as immune cells do not express much, if any NMIIB (Surcel *et al.*, 2015). Further, in some cancer types, such as pancreatic cancer, NMIIB is poorly to undetectably expressed in healthy pancreatic ductal tissue, primary cells, and metastatic cells, which seems contrary to the highly motile and invasive characteristics that these cells must have had to disseminate, invade, and ultimately form metastases (Surcel *et al.*, 2019; Welch and Hurst, 2019). Moreover, it is becoming increasingly appreciated that NMIIs help regulate signaling and metabolic functions, suggesting that NMIIs do more than just reside at the "bottom" of signaling pathways, gene expression programs, and metabolism regulation (Picariello *et al.*, 2019; Surcel and Robinson, 2019; Park *et al.*, 2020; Wang *et al.*, 2021). However, the depths of these relationships remain to be explored.

In this paper, we leverage our knowledge that pancreatic ductal epithelial cells and pancreatic ductal adenocarcinoma cells and tissues do not typically express NMIIB. We introduced wild-type (WT) and mutant forms of NMIIB into a model patient-derived primary pancreatic cancer cell line, Panc10.05. Using this setup as a discovery platform, we then studied the impact of these NMIIB versions on cell morphology, metabolism, mechanics, and gene expression. The WT and mutant forms studied (R709C, S1935A, and S1935D [Ma *et al.*, 2012; Juanes-Garcia *et al.*, 2015; Schiffhauer *et al.*, 2019]) have specific impacts on each of these cellular properties. Notably, expression of the hyperassembled version S1935A, which is a heavy chain mutant that cannot be phosphorylated on the key residue S1935, dramatically shifts the ATP production rate and increases the spare capacity of mitochondrial-mediated ATP production through oxidative phosphorylation (OxPhos). The R709C mutant, which holds onto ADP much longer than WT NMIIB, as well as the heavy chain phosphomimetic S1935D, induces the cell to become more dependent on OxPhos, rather than on glycolysis. Using RNA-seq, we find that each NMIIB WT and mutant version has a significant impact on gene expression, including several factors involved in progrowth pathways and metabolism. Collectively, the results of this study open the door for numerous new avenues of exploration of the function on NMIIs in cells and strongly points toward the integration of myosin II–based contractility on several other cellular systems.

RESULTS

Stable expression of NMIIB constructs in Panc10.05 cells

To determine the impact of NMIIB expression and function on cell behavior, we developed stable Panc10.05 cell lines exogenously expressing WT NMIIB (IIB), a NMIIB motor mutant (R709C) (Kim *et al.*, 2005; Ma *et al.*, 2012), or heavy chain phosphomimetic mutants for altered NMIIB assembly (S1935A and S1935D) (Juanes-Garcia *et al.*, 2015; Schiffhauer *et al.*, 2019) (Figure 1, A and B). It should be noted that the expression levels of each NMIIB variant are slightly different, with S1935A being the highest. However, as will be described below, the impacts of the NMIIB variants are unique and do not simply trend with expression levels. Together, these mutants would allow us to distinguish the impacts of NMIIB assembly state from motor function on cell behavior. The S1935 mutations were designed to increase or decrease NMIIB assembly by inhibiting heavy chain phosphorylation (S1935A) or mimicking heavy chain phosphorylation (S1935D), respectively (Juanes-Garcia *et al.*, 2015; Schiffhauer *et al.*, 2019), without altering motor function. Alternatively, the R709C mutation, which resides in the NMIIB motor domain, leads to increased actin affinity but decreased actin sliding, thereby inhibiting the complete ATPase cycle and motor function (Kim *et al.*, 2005; Ma *et al.*, 2012). Thus, while the motor activity of NMIIB is inhibited with the R709C mutation, no direct alterations in bipolar thick filament (BTF) assembly are predicted to occur.

To confirm whether these mutations had the intended impacts on NMIIB assembly state, we performed cytoskeletal fractionation on stable cell lines (Figure 1C; Supplemental Figure 1A). We found that when WT NMIIB is expressed, ~50% is associated with the cytoskeletal (insoluble) fraction (Supplemental Figure 1A). Introducing the R709C mutations increases NMIIB association with the cytoskeletal fraction to nearly 100% (Supplemental Figure 1A), likely due to the substantially increased actin affinity of this mutation (Kim *et al.*, 2005). However, surprisingly, the S1935 mutations did not behave as anticipated as assessed by this assay. While introduction of the S1935A mutation may mildly increase the NMIIB cytoskeletal fraction association as compared with WT, the S1935D mutation also exhibited significantly higher insolubility (Figure 1C; Supplemental Figure 1A). Given these data, we asked whether the addition of WT and mutant NMIIBs altered the cytoskeletal association of other NMII paralogues, given that coassembly has been previously observed (Beach *et al.*, 2014). We observed that NMIIA association with the cytoskeletal fraction is significantly increased when WT NMIIB, R709C, or S1935A are introduced, while in S1935D, the NMIIA cytoskeletal fraction is significantly decreased relative to the other lines expressing NMIIB proteins (Figure 1D; Supplemental Figure 1B). Additionally, mild increases in NMIIC cytoskeletal fraction association may be observed with the introduction of R709C and S1935A, but not WT NMIIB or S1935D (Figure 1E; Supplemental Figure 1C). However, given the low concentrations of NMIIC in Panc10.05 cells (Surcel *et al.*, 2019) and the variability of this assay, these trends cannot be extrapolated to a mechanistic understanding of NMIIB's relationship to NMIIC in these cell lines. Together, these data indicate that the S1935D mutation leads to increased NMIIB insolubility through means other than altered regulation of NMIIB assembly through S1935 or simple coassembly with NMIIA or NMIIC paralogues.

We next took advantage of the GFP tag on our NMIIB constructs to observe any changes to NMIIB localization (Figure 1F). In line with the cytoskeletal fractionation assays, both R709C and S1835D mutant NMIIB lines have increased NMIIB association with actin fibers. However, while the R709C mutations seems to be more associated with cortical actin, we observe the S1935A NMIIB mutation to have substantial association with ventral stress fibers (Figure 1F). Importantly, for the cytoskeletal fractionation assay, we allow cells to relax for 5 min before lysis to relax stress fibers and observe primarily cortical actin–associated BTFs. Thus, the S1935A associated with stress fibers may not be captured in our cytoskeletal fractionation (Figure 1, C–E). Interestingly, we also observe most of the S1935D mutant NMIIB associated with cortical actin belts at the edge of cell monolayers (Figure 1F). This distribution likely explains why the S1935D shows increased NMIIB cortical actin association in the NMIIB cytoskeletal fractionation assay (Figure 1C). Together, these data suggest that by adding NMIIB phosphomimetic and motor mutants to Panc10.05 cells we have altered more than just NMIIB assembly dynamics, but also localization and NMII paralogue behavior.

Metabolic shifts as an adaptation to introduction of NMIIB mutants

Given our observations that the introduction of NMIIB mutants led to unexpected NMIIB assembly behavior, as well as NMIIB localization and cytoskeletal association of the other NMII paralogues, we hypothesized that the introduction of these NMIIB forms leads to global changes in cellular pathways. Given the relatively recent emergence of data suggesting links between the cytoskeleton and

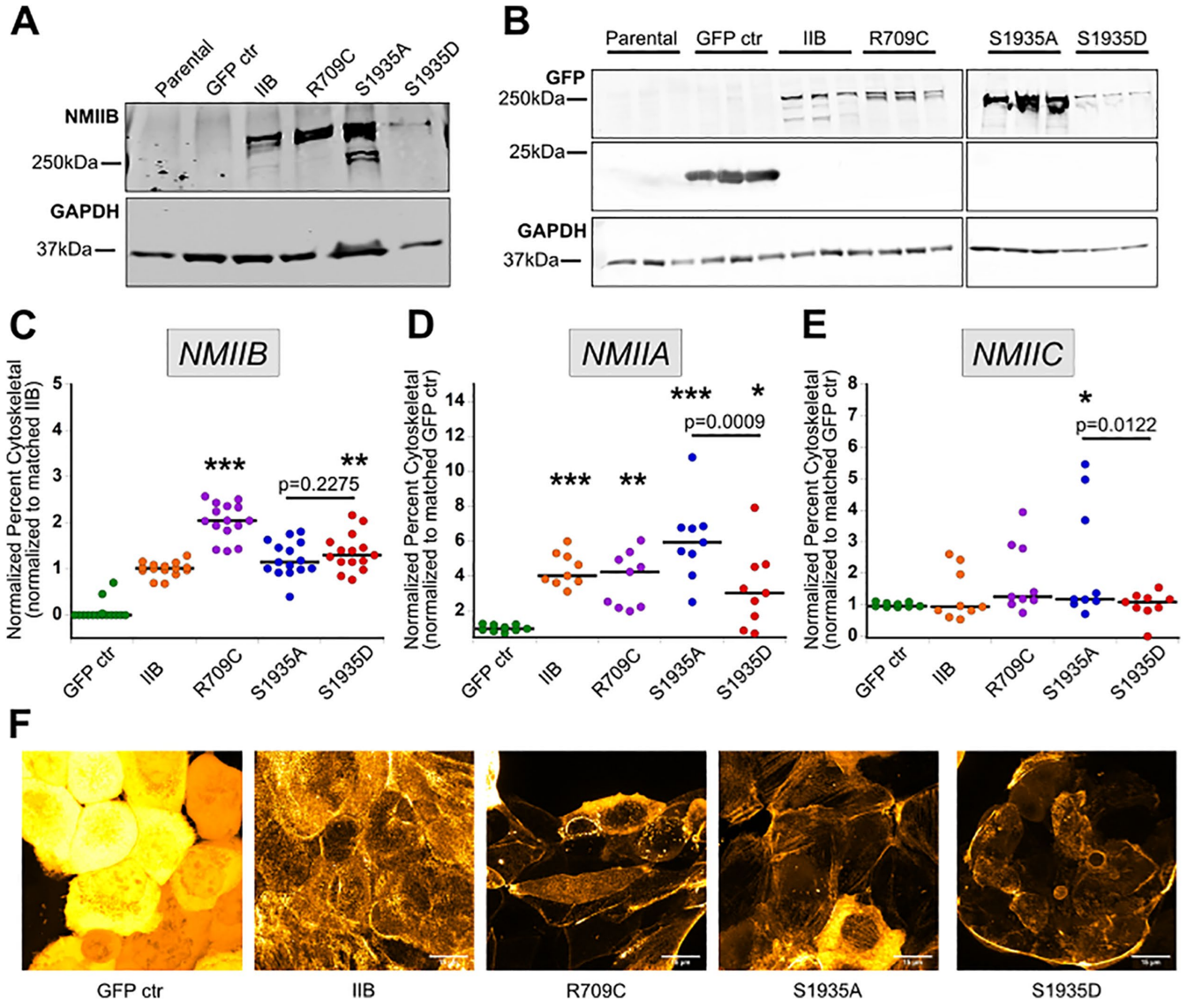

FIGURE 1: NMII cytoskeletal association of Panc10.05 NMIIB stable cell lines. (A) Representative Western blot for GFP-tagged NMIIB, probed with antibody against NMIIB, in Panc10.05 stable lines with GAPDH loading control. (B) Western blot of Panc10.05 stable lines probed for GFP and GAPDH as a loading control. Assay was conducted in biological triplicate with 5×10^4 cells per well. Bars over wells indicate replicates of a cell line. (C) Quantification of GFP-tagged NMIIB cytoskeletal association normalized to matched GFP-NMIIB. Assays were performed in technical triplicate and biological quintuplet with passage-matched cell lines. Outliers were not statistically considered with one-way ANOVA, $p < 0.0001$, followed by Fisher's LSD, $^{**}p < 0.005$, $^{***}p < 0.0001$ compared with the GFP-NMIIB stable line. Outliers are still represented on the graphs. (D, E) Quantification of endogenous NMIIA (D) and NMIIC (E) cytoskeletal association normalized to matched GFP ctrs. Assays were performed in technical and biological triplicate. Outliers were not statistically considered with one-way ANOVA, $p < 0.0001$ (D) and $p = 0.05019$ (E), followed by Fisher's LSD, $^{*}p < 0.05$, $^{**}p < 0.005$, $^{***}p < 0.0001$ compared with GFP ctr. Bars on graphs are medians. Nonnormalized data for panels C–E are provided in Supplemental Figure 1. (F) Representative maximum projections of GFP signal from stable Panc10.05 cells colored using the Orange Hot LUT. Scale bars are 15 μm.

metabolism (Maldonado *et al.*, 2010; Ren *et al.*, 2014; Hu *et al.*, 2016; Bays *et al.*, 2017; Sullivan *et al.*, 2018; Kothari *et al.*, 2019; Park *et al.*, 2020), we tested our hypothesis by exploring changes to cellular metabolism. We first explored whether there were changes in the rate of ATP production in our cell lines. We found that both R709C and S1935D lines exhibited decreased ATP production rates compared with GFP control (GFP ctr) cells (Figure 2A; Supplemental Figure 2A). Thus, we asked whether these lines exhibited altered dependence on ATP production from glycolysis versus OxPhos. Again, we found that those lines that had lower ATP production rates (R709C and S1935D), exhibited an increased dependence on OxPhos over glycolysis for generation of ATP (Figure 2B). We then explored what elements of OxPhos were altered in these cell lines to gain a more mechanistic understanding of the metabolic reprogramming in these lines. For these studies, we utilized Agilent's mitochondrial stress test in which OxPhos-altering drugs are added at distinct time points to distinguish various OxPhos parameters, such as basal respiration, ATP production, maximal respiration, and spare respiratory capacity (Figure 2C). Surprisingly, the most dramatic alteration to OxPhos was the overall increased OxPhos activity in the S1935A

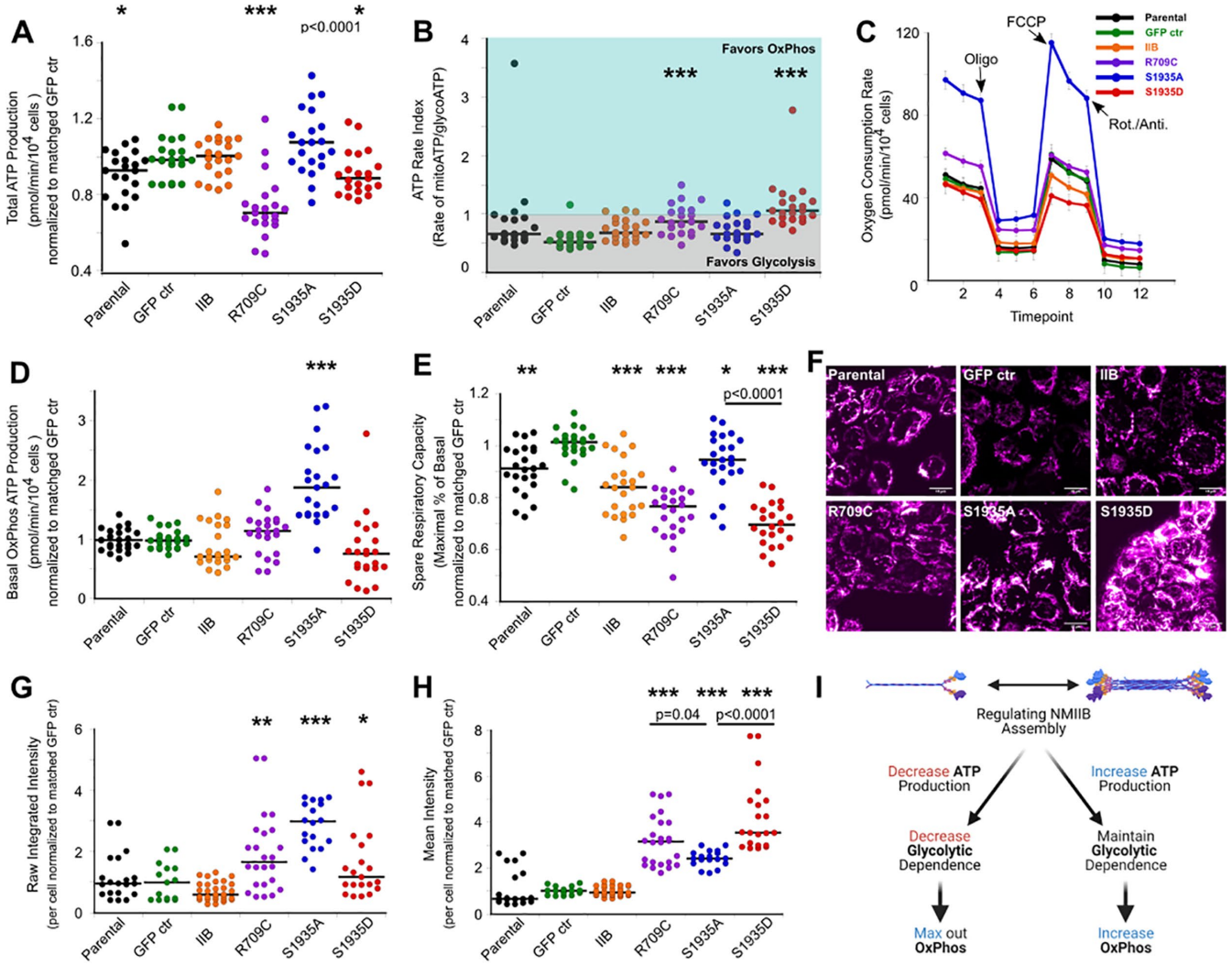

FIGURE 2: NMIIB mutant stable Panc10.05 cells alter OxPhos and mitochondrial mass. (A, B) Seahorse real-time ATP rate assay was used to determine the rate of total ATP production (A) and ATP rate index (B), which is a measure of relative dependency on OxPhos vs. glycolysis for ATP generation. Data are pooled from three biological replicates done in technical septuplet and normalized to matched parental controls. (C–E) Seahorse mitochondrial stress assay was used to determine alterations to OxPhos through addition of molecular moderators (oligomycin, FCCP, and rotenone/antimycin). The test profile with mean and SEM for all lines is shown in C, from which basal OxPhos ATP production (D) and spare respiratory capacity (E) were extrapolated. Data are pooled from three biological replicates done in technical septuplet and normalized to matched parental controls. (F) Representative sum projections of MitoTracker Deep Red FM signal from stable Panc10.05 cells colored using the Magenta Hot LUT. Scale bars are 15 μm. Zoomed-in images are provided in Supplemental Figure 3. (G, H) Quantification of MitoTracker Deep Red FM sum projections for raw integrated intensity (G) and mean intensity (H) per cell normalized to matched GFP ctrs. Per-cell quantification was determined by using DIC images to create the ROIs of cell boundaries and apply them to sum projections. Nonnormalized data for panels A, D, E, G, and H may be found in Supplemental Figure 2. (I) Schematic summarizing metabolic data from figures A–H. Maintenance of NMIIB assembly state results in changes in overall ATP production rates, which are regulated through alterations in glycolytic dependence and OxPhos. Created using BioRender.com. (A–G) Outliers were not statistically considered with one-way ANOVA, $p < 0.0001$, followed by Fisher's LSD, $^{*}p < 0.05$, $^{**}p < 0.005$, $^{***}p < 0.0001$ compared with GFP ctr. (H) Outliers were not statistically considered with Kruskal–Wallis, $p < 0.0001$ followed by Mann–Whitney–Wilcoxon, $^{***}p < 0.0001$ compared with GFP ctr. Outliers are represented on the graphs. Bars on graphs are medians.

line (Figure 2, C and D; Supplemental Figure 2B). However, we also observed a decreased spare respiratory capacity in those lines with decreased ATP production rates and increased dependence on OxPhos (R709C and S1935D) (Figure 2E; Supplemental Figure 2C).

To explore whether changes in OxPhos could be explained by alterations to mitochondrial mass, we used MitoTracker Deep Red FM to image mitochondria in these lines. Using confocal imaging to acquire full Z-volumes, followed by sum intensity projections, we were able to acquire metrics for relative mitochondrial mass per cell (Figure 2, F–H; Supplemental Figures 2, D and E, and 3). We found that R709C and S1935A lines had more mitochondrial mass per cell, as determined by raw integrated density (Figure 2G; Supplemental Figures 2D and 3). However, all three NMIIB mutant lines (R709C, S1935A, and S1935D) had more mitochondria per unit area of the

cell as determined by mean integrated density (Figure 2H; Supplemental Figures 2E and 3). Additionally, while S1935A lines exhibited increased mitochondrial density, compared with controls, the R709C and S1935D lines had significantly higher mitochondrial density than S1935A (Figure 2H; Supplemental Figure 2E). Together, these data suggest that introduction of the R709C and S1935D mutations leads to decreased ATP production, which these cells adapt to by increasing mitochondrial density and/or mass and maxing out OxPhos capabilities to try to meet the ATP production needs (Figure 2I). Alternatively, introduction of the S1935A mutation leads to an increase in ATP production, perhaps due to increased mitochondrial mass that does not alter glycolytic dependence due to increased OxPhos activity (Figure 2I). These data further support the hypothesis that through the introduction of NMIIB mutant forms, large-scale, complex changes to cellular programing have occurred.

NMIIB mutants do not have changes in proliferation but do have changes in cell spreading and size

Owing to the changes in cellular metabolism upon addition of NMIIB mutants, we asked whether metabolic shifts correlated with alterations in proliferation. We found that there were no observable changes in proliferation rates between Panc10.05 stable lines upon plating cells and counting nuclei over time (Figure 3, A and B; Supplemental Figure 4A). However, during these experiments, we observed differences in monolayer morphology (Figure 3C). In particular, S1935A lines became confluent significantly faster than controls, while S1935D took significantly longer (Figure 3, C–E; Supplemental Figure 4B). These data are not entirely explained by changes in cell volume as introduction of WT NMIIB leads to larger cells but decreased surface area coverage compared with controls (Figure 3F; Supplemental Figure 4C). Therefore, the introduction of NMIIB and NMIIB mutants leads to alterations in cell volume and spreading on two-dimensional (2D) substrates.

Impact on cortical tension and mechanoresponsiveness of wild-type and mutant NMIIB variants

To provide further insights into whether mutants of NMIIB display different mechanoresponsive properties and whether these differences lead to changes in the effective cortical tension of cells, we next used micropipette aspiration (MPA) to determine the cortical tension of Panc10.05 cells stably expressing GFP control, myosin IIB, and the mutant variants (Figure 4A). We found that exogenous expression of WT NMIIB led to a reduction in cortical tension as compared with parental and GFP control cells. Interestingly, Panc10.05 cells expressing S1935A also had reduced cortical tension, while those expressing R709C and S1935D were not significantly different from the control lines. In fact, S1935A expression led to the highest reduction in effective cortical tension value (Figure 4B). We next evaluated whether these NMIIB mutants have various abilities to mechanorespond (defined as the ability to accumulate in response to applied stress) as the cells are mechanically challenged with aspiration (Figure 4, C and D). Interestingly, NMIIB with the S1935D mutation had the highest mechanoresponsiveness in response to aspiration, even higher than WT myosin IIB. R709C and S1935A versions did not display the ability to accumulate to aspirated regions. However, the nonresponsive R709C, like the highly responsive S1935D, had a high level of cortical distribution though R709C was slightly more punctated (Figure 4C). In contrast, NMIIB and S1935A were more uniform across the cortex and cytoplasm (Figure 4C). These distribution patterns align well with the distributions of these proteins in adherent cells (Figure 1F). These results suggest that there is a difference in the ability of different versions of NMIIB to contribute to cortical tension and to respond to external forces.

Cellular reprogramming upon stable expression of wild-type and mutant NMIIB

To clarify the cellular processes that had been altered upon addition of WT and mutant NMIIB, we conducted RNA sequencing to explore differential gene expression among these lines (see Supplemental Tables 2–10 for the top 200 up- and down-regulated genes). We found that WT NMIIB and the S1935A mutant had the most changes in gene expression, with the WT NMIIB line favoring up-regulation of genes, while S1935A had a substantial favoring of down-regulated genes compared with the GFP control (Figure 5, A–C). Additionally, the most significantly altered gene expression changes across lines were transcription factors, namely FosB and Notch3. We confirmed FosB expression via Western blotting (Supplemental Table 1; Supplemental Figure 5). In particular, R709C altered FosB to the greatest extent while S1935A and S1935D each similarly negatively impacted FosB expression. Upon hierarchical cluster distance analysis, S1935A and WT NMIIB-expressing lines are the most transcriptionally distinct from controls, while R709C and S1935D are the most like controls and each other (Figure 5, B and C).

To understand the mechanisms that may underlie changes in cellular programming, we looked at changes in transcription factor expression between these lines. To begin this analysis, we looked at the changes in proportion of transcription factor families represented out of the total number of changed transcription factors (Figure 6A; Supplemental Table 11). Interestingly, the number of altered transcription factors is proportional to the number of overall genes with altered expression profiles (Figure 5C vs. Figure 6A). In these analyses, we used the comparison of GFP control to the parental line as an indicator of changes that may be of decreased relevance to those observed with our NMIIB-expressing lines. One of the most dramatic transcription factor family changes was in the homeobox genes, which were dramatically altered, both up- and down-regulated, across cell lines (Figure 6A). Homeobox transcription factors are involved in spatial patterning during embryogenesis and have been documented to be dysregulated in cancer progression (Abate-Shen, 2002). Of particular interest is PBX1, which is a proposed pioneer factor with dysregulation connected to cancer progression, stimulated by glucose, and has direct binding to NMIIs (Macfarlane *et al.*, 1999; Huang *et al.*, 2003; Grebbin and Schulte, 2017). However, PBX1 was altered only in S1935D ($\log_2$(fold change) increase = 1.36)- and WT NMIIB ($\log_2$(fold change) increase = 1.71)-expressing lines. In contrast, a few transcription factors/families were more heavily altered across our panel of cell lines, with differences in both up- and down-regulation. For example, ZBED2 is up-regulated in the WT NMIIB-, R709C-, and S1935D-expressing lines but down-regulated in S1935A (Figure 6A). Interestingly, ZBED2 is the only zf-Bed transcription factor altered in our cell lines, even though at least 12 transcription factors make up this family (Lambert *et al.*, 2018). ZBED2 is increased in PDAC cells, leading to increased motility and invasion as well as suppressed interferon response pathways to promote lineage plasticity (Somerville *et al.*, 2020). Additionally, ESR-like family transcription factors are down-regulated in S1935D and up-regulated in all other NMIIB-expressing lines, while Elf3 (ETS family) is down-regulated in S1935A and up-regulated in all other NMIIB-expressing lines (Figure 6A). Interestingly, ELF3 has been previously described as essential for the mesenchymal-to-epithelial transition, with increased ELF3 associated with the epithelial state (Sengez *et al.*, 2019). These data are

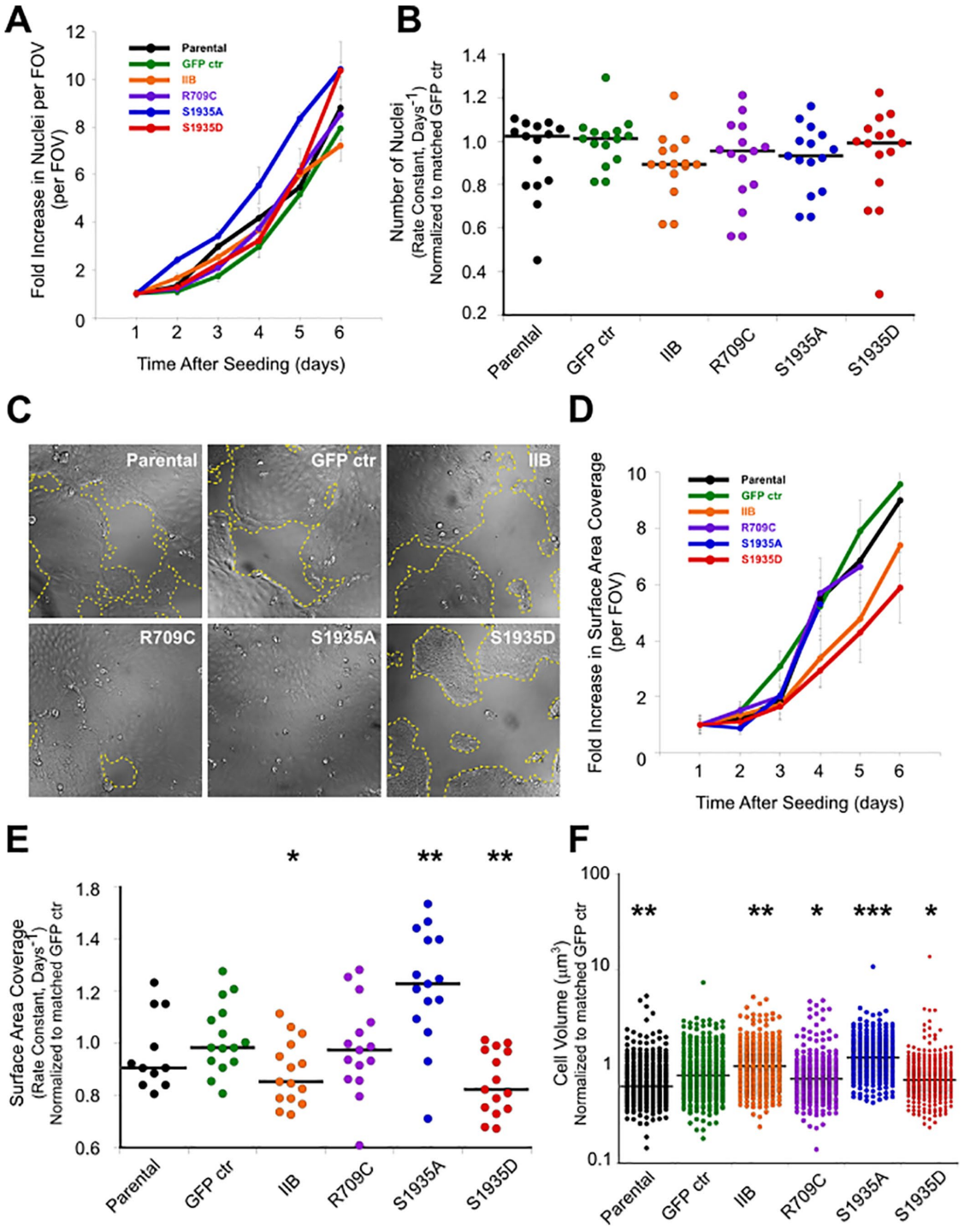

FIGURE 3: Adaptation to exogenous NMIIB expression does not alter proliferation, but cell spreading and size. (A, B) Proliferation rates were determined by imaging and counting nuclei daily for 6 d after seeding Panc10.05 stable cells. Nuclei counts were then plotted over the time course using the median and standard deviation from the nine fields of view (FOV) taken per well per day. A representative example from an experiment is shown in A. These data were then fitted to an exponential curve, and the rate constant from each experiment was plotted as a measure of proliferation rates (B). Data are pooled from four biological replicates done in technical triplicate or quadruplet ($n = 15$) and normalized to matched GFP controls. Outliers were not statistically considered with one-way ANOVA, $p = 0.64104$. (C–E) In the same experiments done in A and B, bright-field images were acquired to quantify the rate of surface area coverage by Panc10.05 stable cells. (C) Representative images from day 5 of an experiment with boundaries of cell monolayers outlined with yellow dashed line. From these images, the percentage of surface area covered by cells was quantified using the PHANTAST macro in Fiji, and the median and standard deviation plotted from nine FOVs per well per day. A representative example from an experiment is shown in D. These data were then fitted to an exponential curve, and the rate constant from each experiment was plotted as a measure of rates of surface area coverage (E). Data are pooled from four biological replicates done in technical triplicate or quadruplet ($N = 15$) and normalized to matched

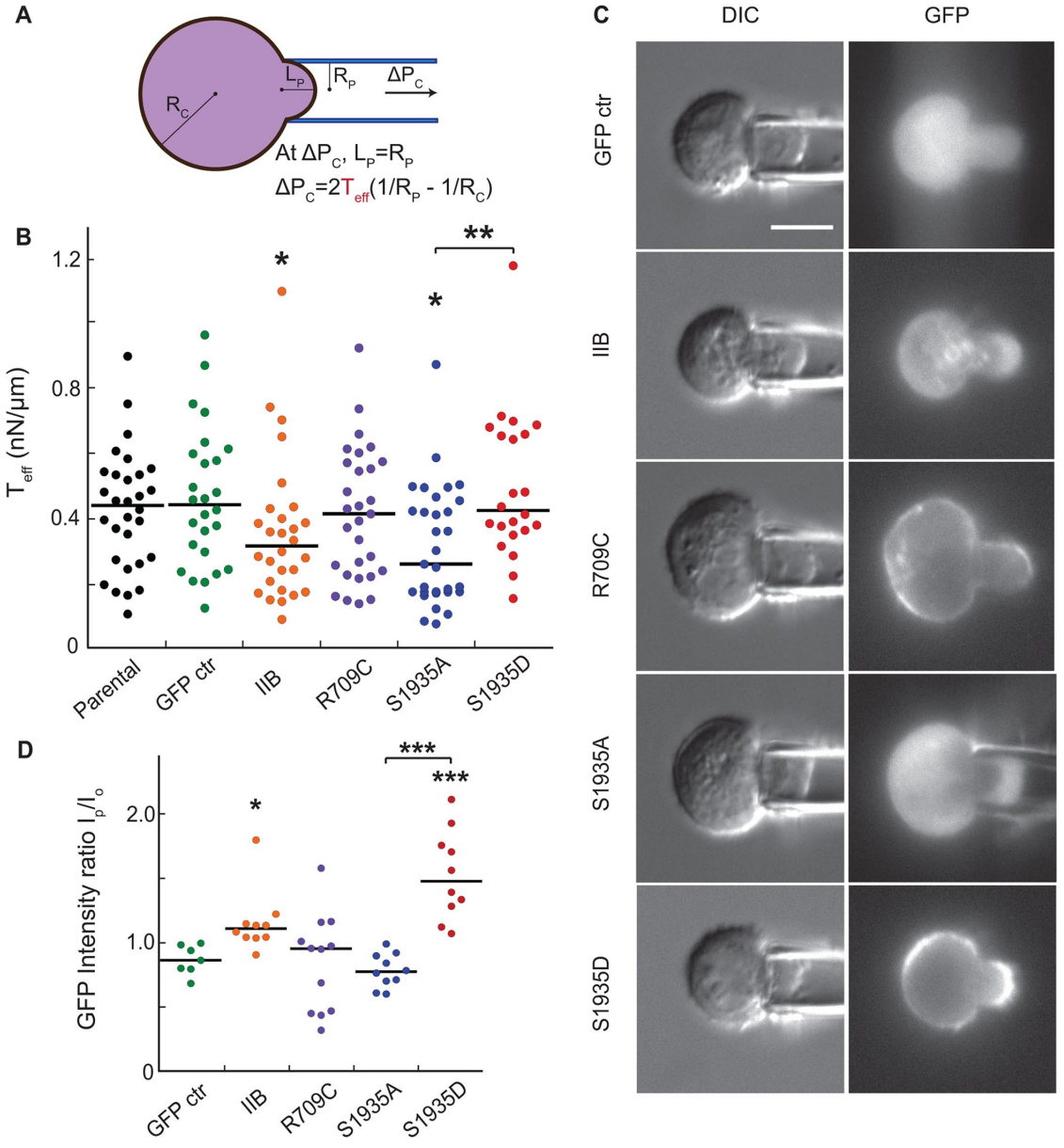

FIGURE 4: Different mutant forms of NMIIB display varying mechanoresponsiveness and differential contributions to Panc10.05 cell's cortical tension. (A) Manipulation of cells by MPA for cortical tension and mechanoresponsiveness analysis. Negative water pressure is gradually increased until the length of the region of the cell inside the pipette (L_p) equals the radius of the cell (R_c). The displayed equation shows how T_{eff} is calculated based on variables extracted from the experiment. (B) Effective cortical tension (T_{eff}) values of Panc10.05 cells expressing exogenous versions of NMIIB, compared with parental cells. (C) DIC and GFP images showing localization and/or mechanoaccumulation of the exogenous GFP-tagged NMIIBs as cells are aspirated with a micropipette. GFP ctr serves as a negative control. Scale bar is 10 μm. (D) The degree of mechanoresponsiveness of GFP-tagged myosin IIBs is quantified as the GFP intensity ratio (I_p/I_o) of the cortex inside the pipette (I_p) to the cortex on the opposite side of the cell (I_o). GFP intensity ratios are compared with those of the GFP control. All *P* values were derived from Kruskal–Wallis followed by the Wilcoxon test (*, $p < 0.05$; **, $p < 0.01$; ***, $p < 0.001$).

GFP controls. Outliers were not statistically considered with one-way ANOVA, $p < 0.0001$, followed by Fisher's LSD, *$p < 0.05$, **$p < 0.005$ compared with GFP ctr. (F) Cell volume was determined by trypsinizing Panc10.05 stable cells, allowing them to relax for 5 min, and then imaging 20 FOVs of rounded cells in suspension. The volume was determined by measuring the diameter of rounded cells and extrapolating volume (see *Materials and Methods*). Data are pooled from two independent experiments and normalized to matched GFP controls. Outliers were not statistically considered with one-way ANOVA, $p < 0.0001$, followed by Fisher's LSD, *$p < 0.05$, **$p < 0.005$, ***$p < 0.0001$ compared with GFP ctr. Outliers are represented in the graphs, and bars are medians. Nonnormalized data for panels B, E, and F may be found in Supplemental Figure 4.

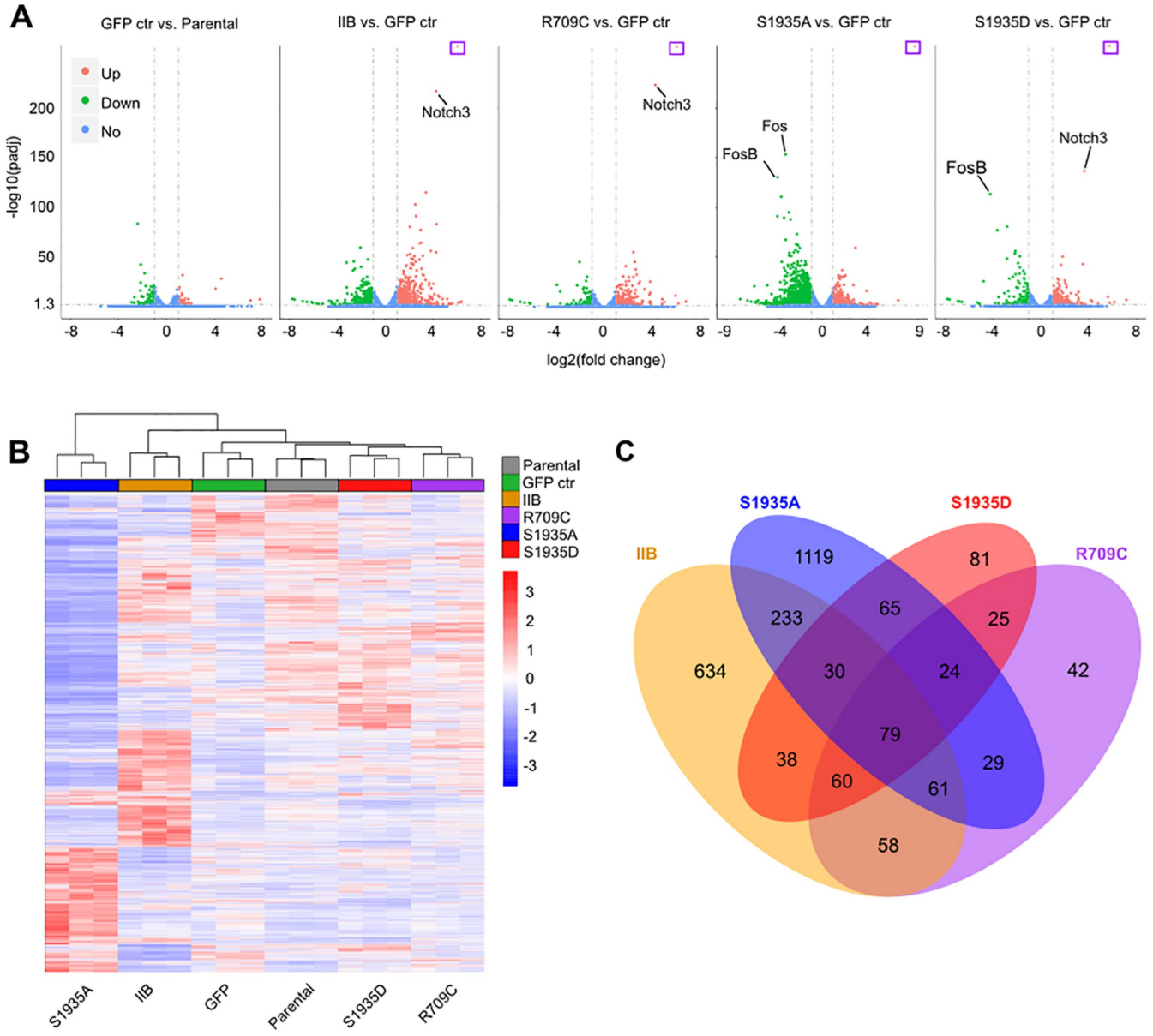

FIGURE 5: Differential gene expression in NMIIB and NMIIB mutants. (A) Volcano plots of differential gene expression analysis between cell lines are shown at the top of the plots. Dashed lines distinguish thresholds for no expression changes (>1-fold change and >1.3 -log10(padj)). Purple boxes indicate NMIIB (MYH10), which was so significantly up-regulated in comparison to GFP ctr that the data point does not fit on the graph. Some of the most significantly altered transcription factors, FosB and Notch3, are indicated with gene names. (B) Heat map generated using the hierarchical clustering distance method on data with >2-fold gene expression change and padj < 0.05. Up-regulated genes are indicated in red and down-regulated in blue. Clustering analysis by cell line is indicated by the dendrogram at the top of the heat map. (C) Venn diagram of genes in NMIIB lines with >2-fold gene expression change and padj < 0.05 when compared with GFP ctr.

aligned with our observations of flattened S1935A cells leading to increased surface area coverage (Figure 3, C and E).

In addition to those transcription factors/families for which we observed changes across all cell lines, we also observed several families in subsets of NMIIB-expressing lines that have altered expression. For example, the ARID, MYB, MH1, THR-like, TSC22, CUT, and Pou transcription factor families have members of altered expression in the WT NMIIB and S1935A lines (Figure 6A). Interestingly, while the THR-like, TSC22, and Pou members are up-regulated when WT NMIIB is expressed, they are down-regulated when S1935A is expressed (Figure 6A). Additionally, HES1, a regulator of epithelial-to-mesenchymal transition and transcriptional repression (Liu *et al.*, 2015), is down-regulated in all NMIIB-expressing cell lines. A subset of transcription factor families is altered in one stable cell line over the others. S1935A shows down-regulation of SAND, p53, NDT80/PhoG, IRF, C/EBP, CSD, ZBTB, CP2, AP2, and STAT family members and up-regulation of GLMP (aka NCU-G1) (Figure 6A). Likewise, S1935D down-regulates GATA6, a member of the zf-GATA family (Figure 6A).

To determine whether transcriptional changes could explain the alterations that we observed in metabolism, we used the mitoXplorer analysis and visualization tool previously reported (Yim *et al.*, 2020).

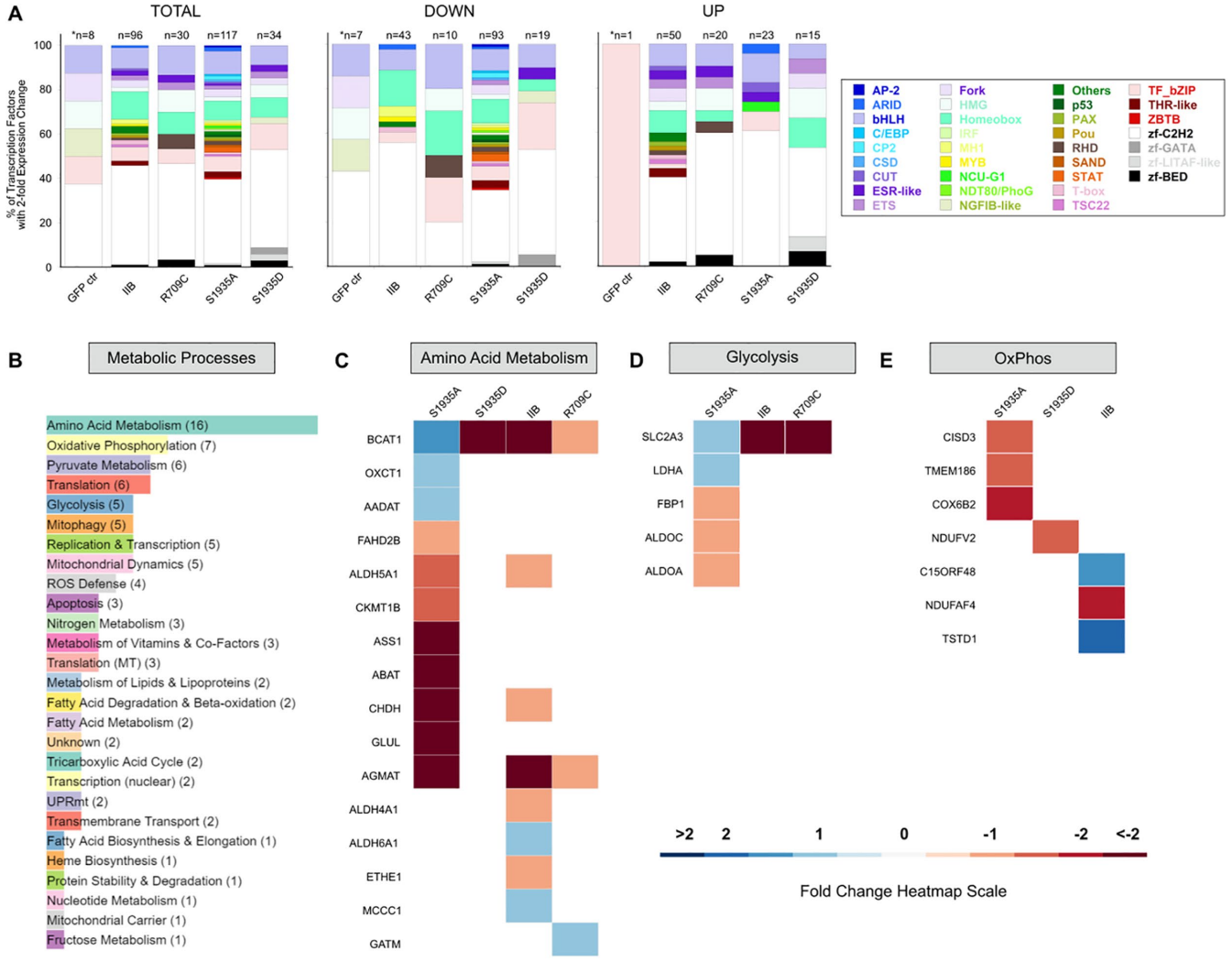

FIGURE 6: Cellular reprogramming upon exogenous expression of NMIIB and NMIIB mutants. (A) Transcription factor families with altered gene expression. The proportion of transcription factors represented by a given family was determined by quantifying the percentage of the total number of transcription factors with altered expression profiles (>2-fold gene expression change and padj < 0.05) represented by a given family. Total numbers of transcription factors with altered expression profiles are indicated at the top of each bar. All NMIIB-expressing lines were compared with the GFP ctr, and the GFP ctr was compared with the parental line, as indicated by *. Families that had altered expression in GFP ctr were deemphasized in the analysis, as indicated by the fainter color schemes. All families with altered gene expression (up- + down-regulated) are represented in the first plot (left), followed by those that are down-regulated (middle) and up-regulated (right). Color codes for a given transcription factor family are indicated. (B–E) Transcriptional changes to metabolic processes in NMIIB-expressing lines as determined by MitoXplorer (Yim *et al.*, 2020) comparing genes from all NMIIB-expressing lines with >2-fold gene expression change and padj < 0.05 compared with GFP ctr. (B) Abundance of changes to genes in the indicated metabolic processes. Number of genes altered across all NMIIB-expressing lines is indicated in parenthesis and visually represented by the length of the colored bar. (C–E) Heat maps indicating fold change in altered gene groups by metabolic pathway: (C) amino acid metabolism, (D) glycolysis, and (E) OxPhos. Gene names are indicated on the left of the corresponding row, with cell lines with altered expression indicated at the top of the column. Scale bar for heat maps is at the bottom.

With this tool, we found that the most abundant changes to metabolism in these cell lines occur in amino acid metabolism (Figure 6B). Of particular interest is branch chain aminotransferase (BCAT1), which is the only gene in the group that has altered expression across all cell lines (elevated in 1935A and reduced in the others) and whose depletion has been linked to decreased OxPhos and glycolysis (Papathanassiu *et al.*, 2017) (Figure 6C). Because our metabolic data centered around changes to glycolysis and OxPhos, we also specifically looked at genes with altered profiles in these pathways (Figure 6, D and E). Importantly, both these pathways were in the top five components of metabolism with altered expression across cell lines (Figure 6B). While no genes were observed to have changes across all cell lines, the glucose transporter SLC2A3 had increased expression in S1935A and decreased expression in the WT NMIIB- and R709C-expressing lines (Figure 6D).

DISCUSSION

While most cell biology research seeks to decipher molecular mechanisms of cellular processes, here we sought to test how the introduction of NMIIB, a major driver of cell motility, into cells that normally

do not express this myosin II, impacts cell behavior. The current study is part of a larger effort to create designer cells with altered mechanical and migratory behaviors. Here, we leveraged our knowledge of an aggressive cancer cell type, pancreatic ductal adenocarcinoma, which does not appreciably express NMIIB (Surcel *et al*., 2019), and introduced NMIIB variants. Upon introduction, the WT, R709C, and S1935D variants were expressed at similar levels, while S1935A was more highly expressed. Yet, each of the variants had its own unique impact and did not track with expression levels. Using this platform, we identify a broad range of changes experienced by cells due to the addition of WT or functional mutant NMIIB. It should be noted that the overall growth of cells was largely unchanged, but morphologies were altered (Figure 3). However, major changes include alterations in morphology, metabolism, and mechanics (Supplemental Table 12). In addition, substantial changes in gene expression were also observed with a few 100 genes having altered expression that differ across the panel of NMIIB mutants.

The introduction of WT NMIIB provides the first insight into the global changes that are experienced by the cell as a result of solely changing this mechanoenzyme. Previously, Engler *et al*. (2006) demonstrated that gene expression was altered by substrate stiffness, with myosin II serving as a mediator of these mechanical cues, which then leads to lineage changes. However, in this paper, we observe changes in cellular programming that are independent of external perturbations or environmental changes. We observed that expression of WT NMIIB increased cell volume and the protein integrated into the cell's stress fiber network and cortex. The metabolic activity remained largely unchanged, but the cell had decreased spare respiratory capacity, indicating that the cells lost some metabolic capacity. Notably, the changes observed are not the result of significant increases in total NMII expression, as NMIIA and NMIIC do not show increased expression (Supplemental Table 13).

The S1935A mutant, which drives the NMIIB into the assembled form (Juanes-Garcia *et al*., 2015), had a major impact on morphology and metabolism. As anticipated, this mutant had an increased insoluble fraction, consistent with the expectation that it would assemble more fully into bipolar filaments (Juanes-Garcia *et al*., 2015; Schiffhauer *et al*., 2019). The cells also acquired enhanced glycolytic and OxPhos modes of metabolism, increasing overall ATP production. These cells also had the largest decrease in cortical tension. This effect may seem paradoxical to the canonical view that NMIIs increase cortical tension and stiffness. However, myosin IIs also promote cytoskeletal dynamics by helping to remodel the cytoskeletal network (Girard *et al*., 2006; Srivastava and Robinson, 2015). Further, cells expressing this overassembled NMIIB had major changes in gene expression, including reduction of progrowth pathways, such as FosB. This collection of observations suggests that the assembled myosin IIB sends the signal that the cell is in a highly active state, requiring additional ATP, and that growth might need to be slowed down until the activities are resolved.

The S1935D mutant unexpectedly had a larger insoluble fraction, suggesting increased assembly and/or lack of solubility. This mutant generally serves as a phosphomimetic, mimicking the phosphorylated version induced by the kinase PKCζ (Juanes-Garcia *et al*., 2015; Schiffhauer *et al*., 2019). However, NMIIB does coassemble with other NMIIs, especially NMIIA (Shutova and Svitkina, 2018), which is very highly expressed in PDAC cells (Surcel *et al*., 2019). Furthermore, in *Dictyostelium*, the phosphomimetic 3xAsp readily coassembles with WT myosin II, though the overall myosin II cellular organization pattern becomes altered (Ren *et al*., 2014). In the Panc10.05 cells, NMIIB S1935D assembled with the actin network and was especially enriched at the cortex as opposed to throughout the cytoplasmic actin network as observed for the WT and S1935A versions. The impact of the phosphomimetic state of S1935D may be that it promotes greater assembly/disassembly dynamics, which helps with cytoskeletal remodeling. Interestingly, 1935D also caused the cells to shift to a more heavily aerobic respiration mode of ATP production, even maxing out ATP production through OxPhos so that the cell had limited spare respiratory capacity. This increase in ATP production is likely reflective of increased NMIIB dynamics in these cells.

Furthermore, the observation that S1935D is a strongly mechanoresponsive NMIIB version when expressed in Panc10.05 cells aligns with our previous observation of a biphasic relationship between the percentage of myosin II assembly state, assembly dynamics, and myosin II's mechanoresponsiveness (Schiffhauer *et al*., 2019). Because Panc10.05 cells are poised at the higher end of the NMIIB assembly state (>20% insoluble), expressing the highly assembled S1935A and R709C mutant proteins cannot push the system any further into a highly mechanoresponsive state. In contrast, when the phosphomimetic S1935D is introduced into cells, the increased NMIIB assembly/disassembly dynamics allow the protein to respond, and the system shifts to a more mechanoresponsive state. One possible explanation for the differential effective cortical tension observed in different myosin IIB mutations is that the S1935D allows for more turnover of the NMIIB, which helps increase the overall dynamics of the cortex. In contrast, the WT and S1935A mutant NMIIBs may remain assembled, allowing the motor domains to remodel the actin meshwork.

The R709C mutant, which slows ADP release, causing the NMIIB to remain associated with actin (Ma *et al*., 2012), had another set of profound impacts. This mutant NMIIB had a nearly 100% association with the insoluble cytoskeletal network, consistent with its characteristic of locking on the actin filaments. By locking onto the actin, this NMIIB mutant may be unable to remodel the actin meshwork, leading to no changes in cortical tension relative to parental or GFP control cells and no mechanoresponsiveness. Moreover, like the S1935D mutant, this protein causes the cell to max out significantly its ability to produce ATP via OxPhos.

Based on the collective impact of the introduction of WT and different mutant NMIIBs, it appears that cells sense and globally respond to NMIIB activity. While the drivers of these responses are yet to be elucidated, cellular morphology, including mechanics and mechanoresponsiveness, and metabolism are downstream responders to NMIIB (Figure 6). These responders may be the result of direct interaction between NMIIB and these cellular programs or indirectly modified due to changes in cellular programming due to gene expression changes.

Significant changes in several families of transcription factors are observed in the developed cell lines. S1935A has the largest overall impact, followed by WT NMIIB. In contrast, the S1935D and R709C mutants have more modest effects in terms of total number of genes impacted. A broad range of families of transcription factors, particularly zinc-finger, homeobox, and basic leucine zipper (bZIP) transcription factors, are retuned in response to the NMIIB variants. As an example, R709C increased FosB while S1935A and S1935D each similarly negatively impacted FosB expression. Many other factors are also altered, along with changes in pathways that govern different modes of metabolism consistent with the significant changes in ATP production through OxPhos and glycolysis.

In all, this study indicates that the activity state of NMIIB, not just the presence or level of the protein, provides a major input into the cell identity and behavioral profile. How many of these changes are compensatory versus directive remains to be determined.

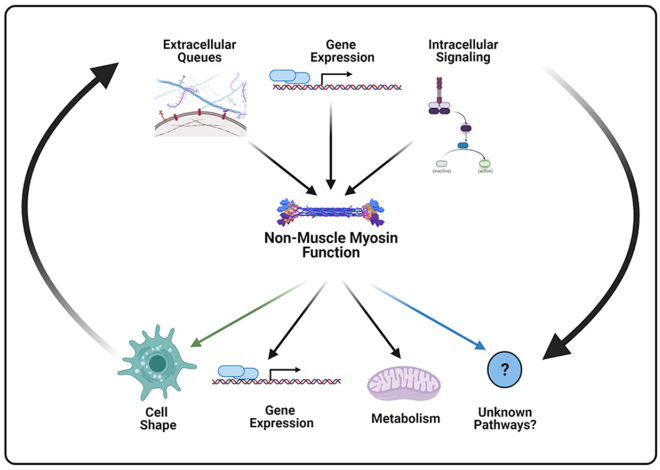

FIGURE 7: Integrated perspective on the role of NMII in cellular processes. The traditional view of NMII's role in cellular biology focuses on myosin function as a downstream effector resulting from extracellular queues, gene expression changes, and/or intracellular signaling events. However, our study, and others, suggest that NMII can be an upstream regulator of a range of cellular processes. NMII's role in regulating cell shape has been extensively appreciated and studied; however, its impact on modulating gene expression, metabolism, and likely other cellular pathways has yet to be thoroughly elucidated. We hypothesize that NMII is both an effector, responding to signals as highlighted by the traditional perspective, but also an affector, initiating signaling cascades, which can alter cellular programming. We suggest that NMII's effector and affector roles are maintained in balance, feeding into one another, to guide cell behavior. Cartoon created with BioRender.

However, the old adage that myosin II simply resides at the bottom of signaling and gene expression pathways and is the benefactor of the cell's metabolic activity, burning the ATP as it conducts contractility, is oversimplified (Figure 7). Instead, NMIIB serves as a director of a wide range of cellular processes, which includes metabolism and gene expression, as well as cortical tension, force production, cytoskeletal organization, and mechanoresponsiveness. In fact, we now are beginning to appreciate that the cellular systems, including all those described here, are fully engaged with each other such that no system is truly at the bottom or top. Perhaps it is better to think of the cell as a highly integrated system where all components fit together to ensure that the machine is fully functional and adaptive to whatever demands that are placed upon it. In summary, this study is an idea generator that opens the door to numerous new studies to explore how these cellular systems interact, integrate, and respond as the cell undergoes its numerous activities and at the same time senses experiences external inputs from its environment.

MATERIALS AND METHODS

Request a protocol through *Bio-protocol*.

Plasmid generation

All mutant NMIIB plasmids were generated using the FastCloning approach outlined in Li *et al.* (2011). GFP-tagged NMIIB (N-terminal label on gene MYH10; Addgene #11348) were gifts from Robert Adelstein (NIH, Bethesda, MD; Wei and Adelstein, 2000). GFP-tagged NMIIB containing S1935D and S1935A mutations were gifts from Miguel Vincente-Manzanares (University of Salamanca, Salamanca, Spain; made by site-directed mutagenesis of the WT NMIIB constructs described above) (Juanes-Garcia *et al.*, 2015). The R709C mutation arose from a random PCR-induced mutation during amplification of unmutated GFP-NMIIB for cloning. All GFP-NMIIB sequences were amplified off the above plasmids using primers containing ~16 base pair overhangs with the lentiviral vector plasmid (pLenti GFP-CMV Hygro [pLenti]; Addgene #17446 [Campeau *et al.*, 2009]), while the pLenti vector was amplified using primers for the opposite strand of the overhangs. After PCR, 1 µl of *Dpn*1 was added directly to 50 µl of unpurified PCR; PCRs for NMIIB sequences and lentiviral vectors were mixed 1:1 and allowed to digest for 1 h at 37°C. Following digestion, 1 µl of each reaction was added to STBL2 cells (100 µl) for a standard transformation protocol. To develop the unmutated NMIIB plasmid, a site-directed mutagenesis approach was used to change the R709C mutation back to the WT sequence. The standard protocol was followed as provided by the New England BioLabs website for the Q5 site-directed mutagenesis kit (#E0554). All plasmids were verified by sequencing the entire NMIIB sequence.

Cell culture

Human primary pancreatic ductal tumor–derived Panc10.05 cell lines were purchased from the American Type Culture Collection (ATCC) and maintained in Panc Media (RPMI 1640, L-glutamine media [Life Technologies #11875093] supplemented with 1% penicillin and streptomycin [Sigma-Aldrich #P0781], sodium pyruvate [Life Technologies #11360070], nonessential amino acids [Life Technologies #11140050], 10% fetal bovine serum [ATLAS Bio], and 0.2% insulin [Life Technologies #12585014]) using standard culture methods. Routine mycoplasma testing was performed using the MycoAlert Mycoplasma Detection Kit (Lonza #LT07-318) every 3–6 mo, and cell lines were grown for no more than 10 passages in all experiments. Additionally, Panc10.05 cell lines were always given at least 2 d to adhere to substrates before experiments were conducted.

Generation of lentiviruses

Lentiviruses were developed by transfecting HEK293T LentiX cells with lentiviral packaging (psPAX2; Addgene #12260, gift from Didier Trono, Swiss Federal Institute of Technology Lausanne, Switzerland) and envelope (pDM2.G; Addgene #12259, gift from Didier Trono) plasmids alongside NMIIB constructs. Briefly, psPAX2 (16.876 µg), pMD2.G (2.767 µg), and NMIIB/GFP control constructs (6.548 µg) were added to 500 µl of Opti-MEM (Life Technologies #31985070). Then 78.57 µl of FuGENE (Promega #E2311) was added to 421.4 µl of Opti-MEM in a separate tube before mixing with DNA containing Opti-MEM followed by brief vortexing. The mixture was then allowed to sit at room temperature for 10 min before being added dropwise to HEK293T LentiX cells at approximately 70% confluency in media without penicillin or streptomycin. Cells were incubated overnight before media was changed and then allowed to incubate for 2 d after which the media was collected and filtered through a 0.45 µm syringe filter to remove cells and then centrifuged at 16,600 rpm at 4°C for 2 h. All but ~500 µl of the supernatant was aspirated, and the viral pellet was left to incubate overnight at 4°C before resuspending the pellet and snap freezing in 100 µl aliquots.

Development of stable lines

All Panc10.05 stable lines were generated in parallel from the same seeding of a low-passage parental Panc10.05 culture at 1.5×10^4 cells/well in a 24-well plate (Falcon #353047). After seeding overnight, media was changed to media without penicillin or streptomycin, and 50 µl of the desired construct containing virus was added to each well. Virus was incubated with cells for 3 d before the

media was changed (without penicillin or streptomycin). Cells were allowed to expand and transferred to larger wells or flasks until enough cells were generated to have 70% confluence in a T75 flask, at which point cells were flow sorted in bulk for GFP expression.

Stable cell lines were confirmed by isolation of genomic DNA using the QIAmp DNA Mini Kit (Qiagen #51304), and exogenously introduced GFP-NMIIB genes were amplified using a touchdown PCR approach. Briefly, LongAmp Taq (NEB #M0323S) was used with a forward primer that binds to GFP (5′-GAGCAAAGACCCCAACGAGA-3′) and a reverse primer that binds to the Woodchuck Hepatitis Virus Posttranscriptional Regulatory Element (WPRE; 3′ to the NMIIB open reading frame within pLenti transfection plasmid) (5′-AGCAGCGTATCCACATAGCG-3′). Annealing temperatures began at 69°C and decreased 2°C per cycle over seven cycles. Then, annealing temperatures were carried out at 54°C for 20 cycles. Specificity of PCR amplification was confirmed by running products on an agarose gel. All PCRs were carried out in duplicate, with duplicates combined for ethanol-based PCR cleanup followed by sequencing of the entire NMIIB open reading frame using the primers in Supplemental Table 1.

Genotyping

All cell lines (parental and genetically modified) used in this study were validated using short tandem repeat profiling with the Johns Hopkins Genetic Resources Core Facility. Briefly, a Promega GenePrint 10 Kit was used to PCR amplify eight short tandem repeat (STR) loci plus a gender-determining marker, Amelogenin. The PCR product was electrophoresed on an ABI Prism 3730xl Genetic Analyzer using an ILS600 internal lane standard (Promega). Data were analyzed using GeneMapper v 4.0 software (Applied Biosystems). An allelic ladder that contains fragments of the same lengths as many of the known alleles for the loci was used to determine the amplified sample fragments alleles. Appropriate positive and negative controls were used. The STR profile was then compared with the profiles on ATCC's website for each cell line.

Cytoskeletal fractionation

Cells were trypsinized and rotated in media for 5 min to allow stress fibers to collapse, primarily leaving behind the cortical actin cytoskeleton that had been allowed to equilibrate following loss of cell adhesion. All cell types were then lysed using a buffer containing 50 mM PIPES, pH 6.8, 46 mM NaCl, 2.5 mM EGTA, 1 mM ATP, 1 mM $MgCl_2$, 0.5% Triton X-100, and a protease inhibitor cocktail (5 μg/ml leupeptin, 1 μg/ml benzamidine, 2 μg/ml pepstatin A, 100 μg/ml Na-p-Tosyl-L-Arginine Methyl Ester hydrochloride (TAME), 80 μg/ml N-p-Tosyl-L-Phenylalanine Chloromethyl Ketone (TPCK), 100 μM Phenylmethylsulfonyl fluoride (PMSF), 150 μM N alpha-Tosyl-L-Lysine-chloromethylketone hydrochloride (TLCK), and 1 μg/ml aprotinin). Samples were then spun at 15,000 × *g* for 10 min at 4°C to separate cytosolic and membranes/cytoskeletal fractions. Sample buffer was added to samples followed by incubation at 95°C for 5 min before spinning through a Qiagen Shredder (#79654) to remove RNA.

Western blots

For quantification of protein expression, cells were lysed at 5×10^6 cells/ml in sample buffer containing protease inhibitor cocktail (5 μg/ml leupeptin, 1 μg/ml benzamidine, 2 μg/ml pepstatin A, 100 μg/ml TAME, and 80 μg/ml TPCK), as well as 100 μM PMSF, 150 μM TLCK, 1 μg/ml aprotonin and 5% 2-Mercaptoethanol. Lysates were heated at 95°C for 5 min before being run through a Qiagen Shredder (#79654) to remove RNA and snap frozen in 23 μl aliquots.

Frozen samples were heated at 95°C for 2 min before being run on 10% SDS–PAGE gels with 15 or 10 μl of cytoskeletal fractionation or protein expression quantification lysates loaded per lane, respectively. Proteins were transferred to nitrocellulose membranes at 90 V for 90 min before blocking with 5% milk/phosphate-buffered saline (PBS) with 0.2% Tween 20 (PBS-T) for 1 h at room temperature. Primary antibodies (see Supplemental Table 1 for sources and dilutions) were diluted in 1% milk/PBS-T and incubated with membranes overnight at 4°C. LiCor fluorescent secondary antibodies (goat anti-mouse, #926-68020; goat anti-rabbit, #926-32211) were diluted 1:10,000 in 1% milk/PBS-T and incubated for 1 h at room temperature before imaging on a LiCor Odyssey CLx system.

Seahorse metabolic tests

Panc10.05 cells were seeded at 1.25×10^5 cells/ml with 80 μl per well in Seahorse cell culture plates (Agilent #101085-VS-PS) 2 d before conducting the assay. On the day before an experiment, the sensor cartridge was hydrated with 200 μl of XF Calibrant (Agilent #100840-000) per well in the utility plate, and the XF media was made by adding 0.5 ml of sodium pyruvate (Agilent #103578-100), L-glutamine (Agilent #103579-100), and glucose (Agilent #103577-100) to 48.5 ml of RPMI without phenol red (Agilent #103576-100). Both the hydrating sensor cartridge and XF media were left in a 37°C incubator with humidity but without CO_2 regulation overnight. On the day of the experiment, cells were washed 1× with XF media by removing 50 μl of old media and adding 150 μl of XF media (final volume 180 μl) and incubated at 37°C in an incubator with humidity but without CO_2 regulation for 1 h. During the incubation, drug stocks were made up in XF media as required for the assay (Cell Mito Stress Test, Agilent #103015; Real-Time ATP Rate, Agilent #103592-100). Each drug (25 μl) was added to the desired port of the sensor cartridge such that the final drug concentrations were as follows: 2 μM oligomycin, 0.25 μM Carbonyl cyanide p-(trifluromethoxy) phenylhydrazone (FCCP), and 0.45 μM rotenone/antimycin A. The sensor cartridge was loaded into the Seahorse system, and the standard protocol was followed for the respective experiments. Before loading the cell microplate, XF media was exchanged as done before. After Seahorse assays were complete, cells were incubated in 2 μM Hoechst for 30 min at 37°C and 5% CO_2 before imaging with a 4× objective on the ImageXpress Micro XLS wide-field high content analysis system (Molecular Devices) to observe nuclei in the entire well. Images were extracted, and nuclei were automatically detected and counted using a custom macro in Fiji (National Institutes of Health). Cell number was then used as a normalization factor for all Seahorse data.

Mitochondrial imaging

Panc10.05 cells were seeded at 2×10^5 cells/ml with 400 μl per well of an eight-chamber coverglass bottom slide (ThermoFisher #155409PK) and allowed to adhere for 2 d. Before imaging, 350 μl of culture media was removed and replaced with 350 μl of phenol red–free culture media (culture media RPMI replaced with Life Technologies #11835030), imaging media, in each well. Then, 4 μl of 100× MitoTracker Deep Red FM (ThermoFisher #M22426) was added to each well and allowed to incubate at 37°C and 5% CO_2 for 30 min. Media was then changed again by removing 350 μl of dye–containing media with 350 μl of fresh imaging media before imaging on a Zeiss AxioObserver with 780-Quasar confocal microscope with 100× oil immersion objective. Z-stacks with 1 μm step sizes were taken to capture the entire cell volume within a field of view with differential interference contrast (DIC) and far-red acquisition. Analysis was conducted in Fiji (National Institutes of Health) on sum

projections of z-stacks by manually creating a region of interest (ROI) using DIC images to trace cell boundaries and then applying those ROIs to the sum projections to extrapolate intensity measurements.

Immunofluorescence assays

To prepare for cell seeding, 12 mm #1 coverslips (Propper) were individually added to wells of a 24-well plate (Falcon #353047) and incubated for 5 min with 100% ethanol followed by three PBS washes. Sterilized coverslips were then incubated for 2 h at 37°C and 5% CO_2 in 50 µg/ml collagen I (rat tail; Life Technologies #A1043-01) in 10 mM (0.1%) acetic acid (filter sterilized). Coverslips were then washed 3× with PBS before adding 4×10^4 cells/ml with 600 µl per well. Cells were allowed to seed for at least 2 d before fixing for 1 h with 4% paraformaldehyde (PFA) at 4°C. Following fixation, coverslips were washed 2× with PBS, and cells were permeabilized with 0.2% cold Triton X-100/1% bovine serum albumin (BSA) (Cell Signaling Technologies #9998) in PBS for 15 min at room temperature followed by three PBS washes. Coverslips were then blocked with 2% BSA/PBS for 30 min at room temperature before three PBS washes and addition of primary antibody diluted in 1% BSA/PBS (see Supplemental Table 1 for a list of antibodies). Cells were incubated in primary antibody for 1 h at room temperature, followed by three PBS washes and addition of secondary antibodies diluted in 1% BSA/PBS. After 1 h of incubation at room temperature, coverslips were washed 3× with PBS before being incubated in 2 µM Hoechst in PBS for 10 min at room temperature. Finally, cells were washed 3× in PBS before mounting coverslips on glass slides with ProLong Diamond Antifade Mountant (Life Technologies #P36961). After Mountant had cured, cells were imaged using a Zeiss AxioObserver with 780-Quasar confocal microscope.

Quantification of proliferation and growth

To determine the proliferation rate and 2D spreading of stable lines, cells were seeded in a 96-well plate (Falcon #353072) with 100 µl of 4×10^4 cells/ml (4000 cells per well) with a full row per cell line. Each day after seeding, 2 µl per well of 200 µM Hoechst was added to one column of wells (final 2 µM) such that one well per cell line was sacrificed when the plate was incubated for 30 min at 37°C and 5% CO_2. The well was then imaged on the ImageXpress Micro XLS wide-field high content analysis system (Molecular Devices) to observe nuclei (4′,6-diamidino-2-phenylindole [DAPI] filter) and cells (bright field) in nine fields of view per well using the 10× objective. This imaging was repeated for 6 d following seeding, and media was changed every other day by replacing 50 µl of media. At the end of the experiment, images were extracted and nuclei and surface area coverage by cells was automatically quantified using custom macros in Fiji. For cell confluency, we customized the PHANTAST macro developed by Jaccard *et al*. (2014) to recognize cell monolayers at different states of confluency.

To determine the volume of stable lines, cells were seeded in six-well plates (Corning #3516) for 2 d before trypsinizing and collecting cell suspensions one-by-one and loading into an observation chamber. Cells were rested for 5 min before imaging 20 random fields of view per line with an Olympus IX71 microscope using an UPanFL 40×1.30 N.A. oil objective and an Andor iXON EMCCD camera. Acquisition was performed using Metamorph software and was analyzed using Fiji (National Institutes of Health). To measure volume, the diameter of all fully visible cells per field of view was measured and volume was extrapolated using the formula $V = \frac{4}{3}\pi r^3$, with $r = \frac{1}{2}(\text{diameter})$, as relaxed trypsinized cells take on a spherical shape.

Micropipette aspiration to measure effective cortical tension and mechanoresponsiveness

A detailed description of our MPA setup has been previously published (Kee and Robinson, 2013). For this study, micropipettes with diameters of 6.5–8.5 µm were forged using the MDI Programmable Multipipette Puller (SKU BZ10133958). The exact radius of each pipette was measured for each experiment. As much as possible, the same pipettes were used across cell lines each day to minimize instrumental variation. Cells were washed once with 1× PBS, trypsinized (0.05% Trypsin-EDTA; Life Technologies) for 5 min and seeded in Panc Media on imaging chambers at approximately 5–10% confluency. Small aspiration pressure was first generated to form attachment between the cell and the pipette tip.

For cortical tension measurements, the pressure was increased until the length (L_p) of the region of the cell pulled into the micropipette equaled the radius of the pipette (R_p). At this point, the equilibrium pressure (ΔP_c) was extracted, and the radius of the cell at that point was quantified. The effective cortical tension T_{eff} was calculated using the Young–Laplace equation:

$$\Delta P_c = 2T_{eff}\left(\frac{1}{R_p} - \frac{1}{R_c}\right)$$

where ΔP_c = aspiration pressure that produced a deformation and where $L_p = R_p$, T_{eff} = effective cortical tension, R_p = radius of the pipette, and R_c = radius of the cell outside the pipette. For the mechanoresponsiveness measurements, cells were slowly aspirated to ~0.40–0.60 nN/µm^2 and held for at least 100 s. Mechanoaccumulation can be observed in the aspirated region at this point. For quantification, the ratio of the background-corrected mean signal intensity of the cortex inside the pipette (I_p) to that of the opposite cortex outside the pipette (I_o) was calculated.

RNA sequencing

All six Panc10.05 stable lines were prepped in parallel at low passage number with three T25 flasks per cell line (i.e., three biological replicates per cell line) used to collect RNA using the Qiagen RNeasy Mini Kit (#74104) with DNase digestion. After isolation of RNA, samples were sent to Novogene (https://en.novogene.com/) for quality control, library preparation, sequencing, and preliminary analysis. Briefly, RNA degradation and contamination were monitored on a 1% agarose gel while purity was checked using the NanoPhotometer spectrophotometer (IMPLEN, USA). RNA integrity and quantitation were assessed using the RNA Nano 6000 Assay Kit of the Bioanalyzer 2100 system (Agilent Technologies, USA). For library preparation, 1 µg of RNA per sample was used to generate libraries with the NEBNext Ultra RNA Library Prep Kit for Illumina (NEB, USA), following the manufacturer's recommendations, and index codes were added to attribute sequences to each sample. mRNA was purified from total RNA using poly-T oligo-attached magnetic beads, and fragmentation was carried out using divalent cations under elevated temperature in NEBNext First Strand Synthesis Reaction Buffer (5×). First, strand cDNA was synthesized using a random hexamer primer and M-MuLV Reverse Transcriptase (RNase H-). Second, strand cDNA synthesis was subsequently performed using DNA polymerase I and RNase H. Remaining overhangs were converted to blunt ends via exonuclease/polymerase activities. After adenylation of the 3′ ends of DNA fragments, NEBNext Adaptor with hairpin loop structure was ligated to prepare for hybridization. To select cDNA fragments of, preferentially, 150–200 base pairs in length, the library fragments were purified with the AMPure XP system

(Beckman Coulter, USA). Then, 3 µl of USER Enzyme (NEB, USA) was used with size, selected, adaptor-ligated cDNA at 37°C for 15 min. followed by 5 min at 95°C before PCR. Next, PCR was performed with Phusion High-Fidelity DNA polymerase, Universal PCR primers, and Index (X) Primer. Finally, PCR products were purified (AMPure XP system), and library quality was assessed on the Agilent Bioanalyzer 21000 system. The clustering of the index-coded samples was performed on an Illumina Novaseq sequencer, according to the manufacturer's instructions. After cluster generation, the libraries were sequenced on the same machine, and paired-end reads were generated. *P* values were adjusted (padj) using the Benjamini and Hochberg's approach for controlling the false discovery rate. Genes with a padj < 0.05 were assigned as differentially expressed.

Statistical analysis

Statistical analysis was performed using KaleidaGraph (Synergy Software). Data sets were first analyzed for outliers (as determined by <Q1–1.5[IQR] and >Q3+1.5[IQR]) and skewness as determined by

$$\frac{\frac{1}{n}\sum_{i=1}^{n}(x_i-\bar{x})^3}{\left(\frac{1}{n}\sum_{i=1}^{n}(x_i-\bar{x})^2\right)^{3/2}}$$

before determining the statistical method (parametric or nonparametric). Parametric data sets were analyzed by analysis of variance (ANOVA) followed by a Fisher's least significant difference (LSD) post hoc test. Nonparametric data sets were analyzed by a Kruskal–Wallis test followed by a Mann–Whitney–Wilcoxon test.

ACKNOWLEDGMENTS

This work was supported by the Defense Advanced Research Projects Agency (HR0011-16-C-0139), National Institutes of Health [NIH] R01 GM66817 and NIH R01 GM149073, and a Johns Hopkins Discovery Award. We also thank the members of the Robinson Lab for their helpful discussions over the course of this project.

REFERENCES

Abate-Shen C (2002). Deregulated homeobox gene expression in cancer: cause or consequence? Nat Rev Cancer 2, 777–785.

Bays JL, Campbell HK, Heidema C, Sebbagh M, DeMali KA (2017). Linking E-cadherin mechanotransduction to cell metabolism through force-mediated activation of AMPK. Nat Cell Biol 19, 724–731.

Beach JR, Shao L, Remmert K, Li D, Betzig E, Hammer JA 3rd (2014). Nonmuscle myosin II isoforms coassemble in living cells. Curr Biol 24, 1160–1166.

Campeau E, Ruhl VE, Rodier F, Smith CL, Rahmberg BL, Fuss JO, Campisi J, Yaswen P, Cooper PK, Kaufman PD (2009). A versatile viral system for expression and depletion of proteins in mammalian cells. PLoS One 4, e6529.

Engler AJ, Sen S, Sweeney HL, Discher DE (2006). Matrix elasticity directs stem cell lineage specification. Cell 126, 677–689.

Girard KD, Kuo SC, Robinson DN (2006). Dictyostelium myosin II mechanochemistry promotes active behavior of the cortex on long time scales. Proc Natl Acad Sci USA 103, 2103–2108.

Grebbin BM, Schulte D (2017). PBX1 as pioneer factor: a case still open. Front Cell Dev Biol 5, 9.

Hu H, Juvekar A, Lyssiotis CA, Lien EC, Albeck JG, Oh D, Varma G, Hung YP, Ullas S, Lauring J, *et al.* (2016). Phosphoinositide 3-kinase regulates glycolysis through mobilization of aldolase from the actin cytoskeleton. Cell 164, 433–446.

Huang H, Paliouras M, Rambaldi I, Lasko P, Featherstone M (2003). Non-muscle myosin promotes cytoplasmic localization of PBX. Mol Cell Biol 23, 3636–3645.

Jaccard N, Griffin LD, Keser A, Macown RJ, Super A, Veraitch FS, Szita N (2014). Automated method for the rapid and precise estimation of adherent cell culture characteristics from phase contrast microscopy images. Biotechnol Bioeng 111, 504–517.

Juanes-Garcia A, Chapman JR, Aguilar-Cuenca R, Delgado-Arevalo C, Hodges J, Whitmore LA, Shabanowitz J, Hunt DF, Horwitz AR, Vicente-Manzanares M (2015). A regulatory motif in nonmuscle myosin II-B regulates its role in migratory front-back polarity. J Cell Biol 209, 23–32.

Kee YS, Robinson DN (2013). Micropipette aspiration for studying cellular mechanosensory responses and mechanics. Methods Mol Biol 983, 367–382.

Kim KY, Kovacs M, Kawamoto S, Sellers JR, Adelstein RS (2005). Disease-associated mutations and alternative splicing alter the enzymatic and motile activity of nonmuscle myosins II-B and II-C. J Biol Chem 280, 22769–22775.

Kothari P, Srivastava V, Aggarwal V, Tchernyshyov I, Van Eyk JE, Ha T, Robinson DN (2019). Contractility kits promote assembly of the mechanoresponsive cytoskeletal network. J Cell Sci 132, 1–12.

Lambert SA, Jolma A, Campitelli LF, Das PK, Yin Y, Albu M, Chen X, Taipale J, Hughes TR, Weirauch MT (2018). The human transcription factors. Cell 172, 650–665.

Li C, Wen A, Shen B, Lu J, Huang Y, Chang Y (2011). FastCloning: a highly simplified, purification-free, sequence- and ligation-independent PCR cloning method. BMC Biotechnol 11, 92.

Liu ZH, Dai XM, Du B (2015). Hes1: a key role in stemness, metastasis and multidrug resistance. Cancer Biol Ther 16, 353–359.

Ma X, Kovacs M, Conti MA, Wang A, Zhang Y, Sellers JR, Adelstein RS (2012). Nonmuscle myosin II exerts tension but does not translocate actin in vertebrate cytokinesis. Proc Natl Acad Sci USA 109, 4509–4514.

Macfarlane WM, McKinnon CM, Felton-Edkins ZA, Cragg H, James RF, Docherty K (1999). Glucose stimulates translocation of the homeodomain transcription factor PDX1 from the cytoplasm to the nucleus in pancreatic beta-cells. J Biol Chem 274, 1011–1016.

Maldonado EN, Patnaik J, Mullins MR, Lemasters JJ (2010). Free tubulin modulates mitochondrial membrane potential in cancer cells. Cancer Res 70, 10192–10201.

Melli L, Billington N, Sun SA, Bird JE, Nagy A, Friedman TB, Takagi Y, Sellers JR (2018). Bipolar filaments of human nonmuscle myosin 2-A and 2-B have distinct motile and mechanical properties. eLife 7, e32871.

Norstrom MF, Smithback PA, Rock RS (2010). Unconventional processive mechanics of non-muscle myosin IIB. J Biol Chem 285, 26326–26334.

Papathanassiu AE, Ko JH, Imprialou M, Bagnati M, Srivastava PK, Vu HA, Cucchi D, McAdoo SP, Ananieva EA, Mauro C, Behmoaras J (2017). BCAT1 controls metabolic reprogramming in activated human macrophages and is associated with inflammatory diseases. Nat Commun 8, 16040.

Park JS, Burckhardt CJ, Lazcano R, Solis LM, Isogai T, Li L, Chen CS, Gao B, Minna JD, Bachoo R, *et al.* (2020). Mechanical regulation of glycolysis via cytoskeleton architecture. Nature 578, 621–626.

Picariello H, Kenchappa R, Rai V, Crish J, Dovas A, Pogoda K, McMahon M, Bell E, Chandrasekharan U, Luu A, *et al.* (2019). Myosin IIA suppresses glioblastoma development in a mechanically-sensitive manner. Proc Natl Acad Sci USA 116, 15550–15559.

Ren Y, West-Foyle H, Surcel A, Miller C, Robinson DN (2014). Genetic suppression of a phosphomimic myosin II identifies system-level factors that promote myosin II cleavage furrow accumulation. Mol Biol Cell 25, 4150–4165.

Schiffhauer ES, Ren Y, Iglesias VA, Kothari P, Iglesias P, Robinson DN (2019). Myosin IIB assembly state determines its mechanosensitive dynamics. J Cell Biol 218, 895–908.

Sengez B, Aygun I, Shehwana H, Toyran N, Tercan Avci S, Konu O, Stemmler MP, Alotaibi H (2019). The transcription factor Elf3 Is essential for a successful mesenchymal to epithelial transition. Cells 8, 858.

Shutova MS, Svitkina TM (2018). Mammalian nonmuscle myosin II comes in three flavors. Biochem Biophys Res Commun 506, 394–402.

Somerville TDD, Xu Y, Wu XS, Maia-Silva D, Hur SK, de Almeida LMN, Preall JB, Koo PK, Vakoc CR (2020). ZBED2 is an antagonist of interferon regulatory factor 1 and modifies cell identity in pancreatic cancer. Proc Natl Acad Sci USA 117, 11471–11482.

Srivastava V, Robinson DN (2015). Mechanical stress and network structure drive protein dynamics during cytokinesis. Curr Biol 25, 663–670.

Sullivan WJ, Mullen PJ, Schmid EW, Flores A, Momcilovic M, Sharpley MS, Jelinek D, Whiteley AE, Maxwell MB, Wilde BR, *et al.* (2018). Extracellular matrix remodeling regulates glucose metabolism through TXNIP destabilization. Cell 175, 117–132.e121.

Surcel A, Ng WP, West-Foyle H, Zhu Q, Ren Y, Avery L, Krenc AK, Meyers D, Rock RS, Anders RA, *et al.* (2015). Pharmacological activation of myosin

II paralogs to correct cell mechanics defects. Proc Natl Acad Sci USA 112, 1428–1433.
Surcel A, Robinson DN (2019). Meddling with myosin's mechanobiology in cancer. Proc Natl Acad Sci USA 116, 15322–15323.
Surcel A, Schiffhauer ES, Thomas D, Zhu Q, DiNapoli K, Herbig M, Otto O, Guck J, Jaffee EM, Iglesias PA, *et al*. (2019). Targeting mechanoresponsive proteins in pancreatic cancer: 4-hydroxyacetophenone blocks dissemination and invasion by activating MYH14. Cancer Res 79, 4665–4678.
Wang Z, Zhu Z, Li C, Zhang Y, Li Z, Sun S (2021). NMIIA promotes tumorigenesis and prevents chemosensitivity in colorectal cancer by activating AMPK/mTOR pathway. Exp Cell Res 398, 112387.
Wei Q, Adelstein RS (2000). Conditional expression of a truncated fragment of nonmuscle myosin II-A alters cell shape but not cytokinesis in HeLa cells. Mol Biol Cell 11, 3617–3627.
Welch DR, Hurst DR (2019). Defining the hallmarks of metastasis. Cancer Res 79, 3011–3027.
Yim A, Koti P, Bonnard A, Marchiano F, Durrbaum M, Garcia-Perez C, Villaveces J, Gamal S, Cardone G, Perocchi F, *et al*. (2020). mitoXplorer, a visual data mining platform to systematically analyze and visualize mitochondrial expression dynamics and mutations. Nucleic Acids Res 48, 605–632.

Supplementary Materials

Molecular Biology of the Cell

Balaban *et al*.

Non-muscle myosin IIB is a driver of cellular reprogramming

Amanda E. Balaban, Ly T.S. Nguyen, Eleana Parajón, and Douglas N. Robinson

Supplemental Materials

Supplemental Materials includes 5 Supplemental Figures and 13 Supplemental Tables.

Supplemental Figures

Sup. Fig. 1. NMII cytoskeletal association of Panc10.05 NMIIB stable cell lines. (A) Quantification of GFP-tagged NMIIB cytoskeletal association. Assays were performed in technical triplicate and biological quintuplet with passage matched cell lines. Outliers were not statistically considered with one-way ANOVA $p<0.0001$, followed by Fisher's LSD *$p<0.05$, ***$p<0.0001$ compared to GFP-NMIIB stable line. Outliers are still represented on graphs. **(B-C)** Quantification of endogenous NMIIA (D) and NMIIC (E) cytoskeletal association. Assays were performed in technical and biological triplicate. Outliers were not statistically considered with one-way ANOVA $p=0.00016$ (B) and $p=0.00451$ (C), followed by Fisher's LSD *$p<0.05$, **$p<0.005$, ***$p<0.0001$ compared to GFP ctr. Bars on graphs are medians.

Sup. Fig. 2. NMIIB mutant stable Panc10.05 cells alter OxPhos and mitochondrial mass. (A) Seahorse Real-Time ATP Rate assay was used to determine rate of total ATP production (A) and ATP Rate Index. Data are pooled from three biological replicates done in technical septuplet. **(B-E)** Seahorse Mitochondrial Stress assay was used to determine alterations to OxPhos through addition of molecular moderators (oligomycin, FCCP, and rotenone/antimycin). Basal OxPhos ATP production (D) and spare respiratory capacity (E) were extrapolated from the oxygen consumption rate profiles (see Fig. 2 for example). Data are pooled from three biological replicates done in technical septuplet. (A-E) Outliers were not statistically considered with one-way ANOVA $p<0.0001$, followed by Fisher's LSD *$p<0.05$, **$p<0.005$, ***$p<0.0001$ compared to GFP ctr. (H) Outliers were not statistically considered with Kruskal-Wallis $p<0.0001$ followed by Mann-Whitney-Wilcoxon ***$p<0.0001$ compared to GFP ctr. Outliers are still represented on graphs. Bars on graphs are medians.

Sup. Fig. 3. Zoomed-in images of mitochondria in cells expressing NMII variants. Merged, MitoRed, transmission photomultiplier tube (tPMT; bright field), and DAPI images are provided. Parental cells and cells expressing GFP are provided as controls. Scale bars are 10 µm.

Sup. Fig. 4. Adaptation to exogenous NMIIB expression does not alter proliferation, but cell spreading and size. (A-B) Proliferation rates were determined by imaging and counting nuclei daily for 6 days after seeding Panc10.05 stable cells. Nuclei counts were then plotted over the time course using the median and standard deviation from the nine fields of view (FOV) taken per well per day. These data were then to an exponential curve and the rate constant from each experiment was plotted as a measure of proliferation rates (A). Data are pooled from four biological replicates done in technical triplicate or quadruplet (n=15). Outliers were not statistically considered with one-way ANOVA $p=0.35866$. **(B)** In the same experiments done in (A), bright field images were acquired to quantify the rate of surface area coverage by Panc10.05 stable cells. From these images, the percent of surface area covered by cells was quantified using the PHANTAST macro in fiji and plotted the median and standard deviation from nine FOVs per well per day. These data were then to an exponential curve and the rate constant from each experiment was plotted as a measure of rates of surface area coverage (B). Data are pooled from four biological replicates done in technical triplicate or quadruplet (n-15). Outliers were not statistically considered with one-way ANOVA $p<0.0001$, followed by Fisher's LSD *$p<0.05$, **$p<0.005$ compared to GFP ctr. **(C)** Cell volume was determined by trypsinizing Panc10.05 stable cells, allowing them to relax for 5 minutes, and then imaging 20 FOVs of rounded cells in suspension. Volume was determined by measuring the diameter of rounded cells and extrapolating volume (see methods). Data are pooled from two independent experiments. Outliers were not statistically considered with one-way ANOVA $p<0.0001$, followed by Fisher's LSD ***$p<0.0001$ compared to GFP ctr. Outliers are still represented in graphs and bars are medians.

Sup. Fig. 5. FosB expression is reduced when NMIIB S1935A and S1935D are introduced. Top row, Western analysis is conducted to detect FosB expression. GAPDH is probed for a loading control. Middle row, Image of the Coomassie stained gel corresponding to the western blot in the top row. Bottom row, Quantification of the western by normalizing the integrated signal to the GAPDH signal after background subtraction.

Supplemental Tables

Sup. Table 1: Antibody and Oligonucleotides used in this study. For each antibody, the isotype, assay used in, dilution, source, and catalogue number are documented. Cyto. Frac. = cytoskeletal fractionation assay. In the bottom half, the name and sequence of oligonucleotides used for sequencing GFP-NMIIB are shown.

Sup. Table 2: Top 200 upregulated and downregulated transcripts in GFP ctr compared to parental (WT). Two tabs are present in this excel sheet, one for downregulated transcripts (labeled: "Top 200 Down") and one for upregulated transcripts (labeled "Top 200 Up"). These tables were generated from the full list of genes with padj <0.05 and >2-fold change in expression. From these data, the top 200 up or down regulated transcripts were determined by magnitude of the $\log_2$[Fold Change]. Together, these two lists do not cover the complete list of altered gene expression.

Sup. Table 3: Top 200 upregulated and downregulated transcripts in wildtype NMIIB compared to GFP ctr. Two tabs are present in this excel sheet, one for downregulated transcripts (labeled: "Top 200 Down") and one for upregulated transcripts (labeled "Top 200 Up"). These tables were generated from the full list of genes with padj <0.05 and >2-fold change in expression. From these data, the top 200 up or down regulated transcripts were determined by magnitude of the $\log_2$[Fold Change]. Together, these two lists do not cover the complete list of altered gene expression.

Sup. Table 4: Top 200 upregulated and downregulated transcripts in R709C compared to GFP ctr. Two tabs are present in this excel sheet, one for downregulated transcripts (labeled: "Top 200 Down") and one for upregulated transcripts (labeled "Top 200 Up"). These tables were generated from the full list of genes with padj <0.05 and >2-fold change in expression. From these data, the top 200 up or down regulated transcripts were determined by magnitude of the $\log_2$[Fold Change]. Together, these two lists do not cover the complete list of altered gene expression.

Sup. Table 5: Top 200 upregulated and downregulated transcripts in S1935A compared to GFP ctr. Two tabs are present in this excel sheet, one for downregulated transcripts (labeled: "Top 200 Down") and one for upregulated transcripts (labeled "Top 200 Up"). These tables were generated from the full list of genes with padj <0.05 and >2-fold change in expression. From these data, the top 200 up or down regulated transcripts were determined by magnitude of the $\log_2$[Fold Change]. Together, these two lists do not cover the complete list of altered gene expression.

Sup. Table 6: Top 200 upregulated and downregulated transcripts in S1935D compared to GFP ctr. Two tabs are present in this excel sheet, one for downregulated transcripts (labeled: "Top 200 Down") and one for upregulated transcripts (labeled "Top 200 Up"). These tables were generated from the full list of genes with padj <0.05 and >2-fold change in expression. From these data, the top 200 up or down regulated transcripts were determined by magnitude of the $\log_2$[Fold Change]. Together, these two lists do not cover the complete list of altered gene expression.

Sup. Table 7: Top 200 upregulated and downregulated transcripts in R709C compared to wildtype NMIIB. Two tabs are present in this excel sheet, one for downregulated transcripts (labeled: "Top 200 Down") and one for upregulated transcripts (labeled "Top 200 Up"). These tables were generated from the full list of genes with padj <0.05 and >2-fold change in expression. From these data, the top 200 up or down regulated transcripts were determined by magnitude of the $\log_2$[Fold Change]. Together, these two lists do not cover the complete list of altered gene expression.

Sup. Table 8: Top 200 upregulated and downregulated transcripts in S1935A compared to wildtype NMIIB. Two tabs are present in this excel sheet, one for downregulated transcripts (labeled: "Top 200 Down") and one for upregulated transcripts (labeled "Top 200 Up"). These tables were generated from the full list of genes with padj <0.05 and >2-fold change in expression. From these data, the top 200 up or down regulated transcripts were

determined by magnitude of the log_2[Fold Change]. Together, these two lists do not cover the complete list of altered gene expression.

Sup. Table 9: Top 200 upregulated and downregulated transcripts in S1935D compared to wildtype NMIIB. Two tabs are present in this excel sheet, one for downregulated transcripts (labeled: "Top 200 Down") and one for upregulated transcripts (labeled "Top 200 Up"). These tables were generated from the full list of genes with padj <0.05 and >2-fold change in expression. From these data, the top 200 up or down regulated transcripts were determined by magnitude of the log_2[Fold Change]. Together, these two lists do not cover the complete list of altered gene expression.

Sup. Table 10: Top 200 upregulated and downregulated transcripts in S1935A compared to S1935D. Two tabs are present in this excel sheet, one for downregulated transcripts (labeled: "Top 200 Down") and one for upregulated transcripts (labeled "Top 200 Up"). These tables were generated from the full list of genes with padj <0.05 and >2-fold change in expression. From these data, the top 200 up or down regulated transcripts were determined by magnitude of the log_2[Fold Change]. Together, these two lists do not cover the complete list of altered gene expression.

Sup. Table 11: Transcription factor families with altered gene expression. Three tabs are presented in this excel sheet, one with has all transcription factors/families (labeled: "Total"), one only the down regulated transcription factors/families (labeled: "Down"), and one with only the up regulated transcription factors/families (labeled: "Up"). Log_2[Fold Change], p-value (pval), padj, gene name (gene), and transcription factor family (tf fam) are shown for each cell line differential gene expression comparison which is indicated in the 1st row. Differential transcription factor expression is shown for GFP vs. parental to identify changes which are unlikely to be specifically due to exogenous expression of NMIIB constructs. Those genes differentially regulated in GFP ctr compared to the parental are colored in light grey on the gene list for each NMIIB construct comparison GFP ctr to indicate this lack of specificity to the NMIIB construct expression. After the lists of differentially expressed transcription factors are the analysis of changes in transcription factor families. First is a count of the total number of altered transcription factors in each family (labeled: "# of Changed TF") for each tab condition (total, down, or up). Then is the percent of altered transcription factors (taking total number from "# of Changed TF" for each respective column) in each family (labeled: "% of Total TF Changed") for each tab condition (total, down, or up).

Sup. Table 12. Summary of Phenotypes vs. Strain/NMIIB Variant.

Sup. Table 13. Endogenous NMII expression is not increased by exogenous NMIIB expression. Mean fragments per kilobase million (fpkm) counts and as well as fpkm reads normalized to the parental control are shown from triplicates used in RNAseq study.

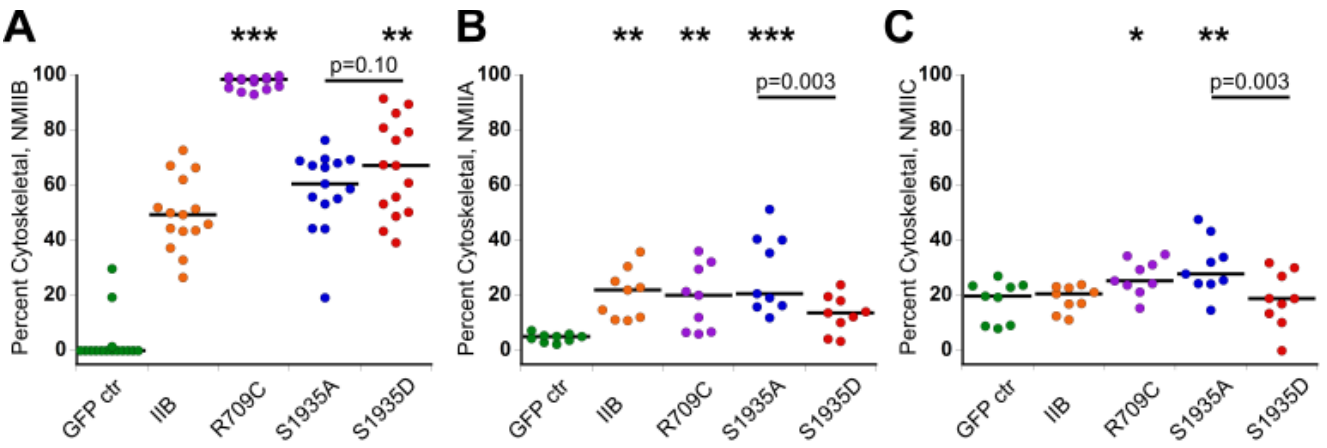

Sup. Fig. 1. NMII cytoskeletal association of Panc10.05 NMIIB stable cell lines. (A) Quantification of GFP-tagged NMIIB cytoskeletal association. Assays were performed in technical triplicate and biological quintuplet with passage matched cell lines. Outliers were not statistically considered with one-way ANOVA p<0.0001, followed by Fisher's LSD *p<0.05, ***p<0.0001 compared to GFP-NMIIB stable line. Outliers are still represented on graphs. **(B-C)** Quantification of endogenous NMIIA (D) and NMIIC (E) cytoskeletal association. Assays were performed in technical and biological triplicate. Outliers were not statistically considered with one-way ANOVA p=0.00016 (B) and p=0.00451 (C), followed by Fisher's LSD *p<0.05, **p<0.005, ***p<0.0001 compared to GFP ctr. Bars on graphs are medians.

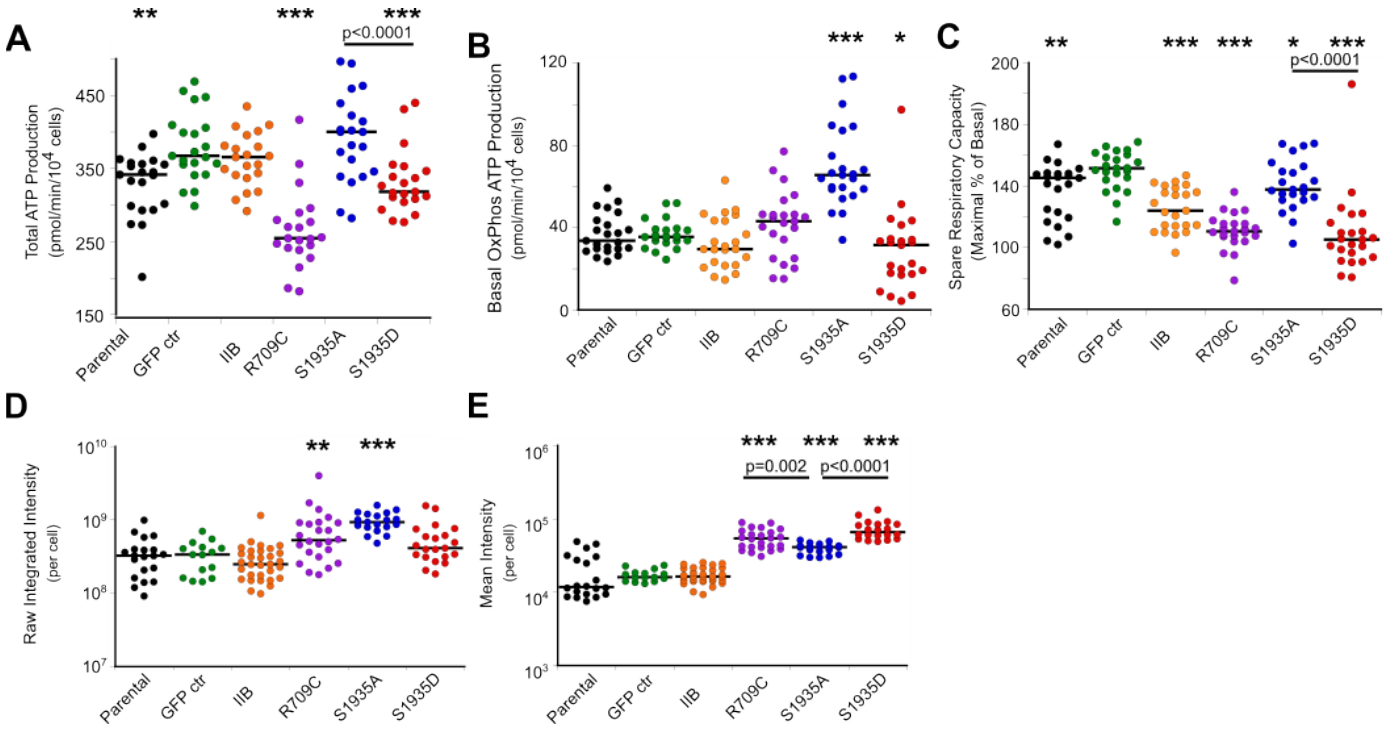

Sup. Fig. 2. NMIIB mutant stable Panc10.05 cells alter OxPhos and mitochondrial mass. (A) Seahorse Real-Time ATP Rate assay was used to determine rate of total ATP production (A) and ATP Rate Index. Data are pooled from three biological replicates done in technical septuplet. **(B-E)** Seahorse Mitochondrial Stress assay was used to determine alterations to OxPhos through addition of molecular moderators (oligomycin, FCCP, and rotenone/antimycin). Basal OxPhos ATP production (D) and spare respiratory capacity (E) were extrapolated from the oxygen consumption rate profiles (see Fig. 2 for example). Data are pooled from three biological replicates done in technical septuplet. (A-E) Outliers were not statistically considered with one-way ANOVA p<0.0001, followed by Fisher's LSD *p<0.05, **p<0.005, ***p<0.0001 compared to GFP ctr. (H) Outliers were not statistically considered with Kruskal-Wallis p<0.0001 followed by Mann-Whitney-Wilcoxon ***p<0.0001 compared to GFP ctr. Outliers are still represented on graphs. Bars on graphs are medians.

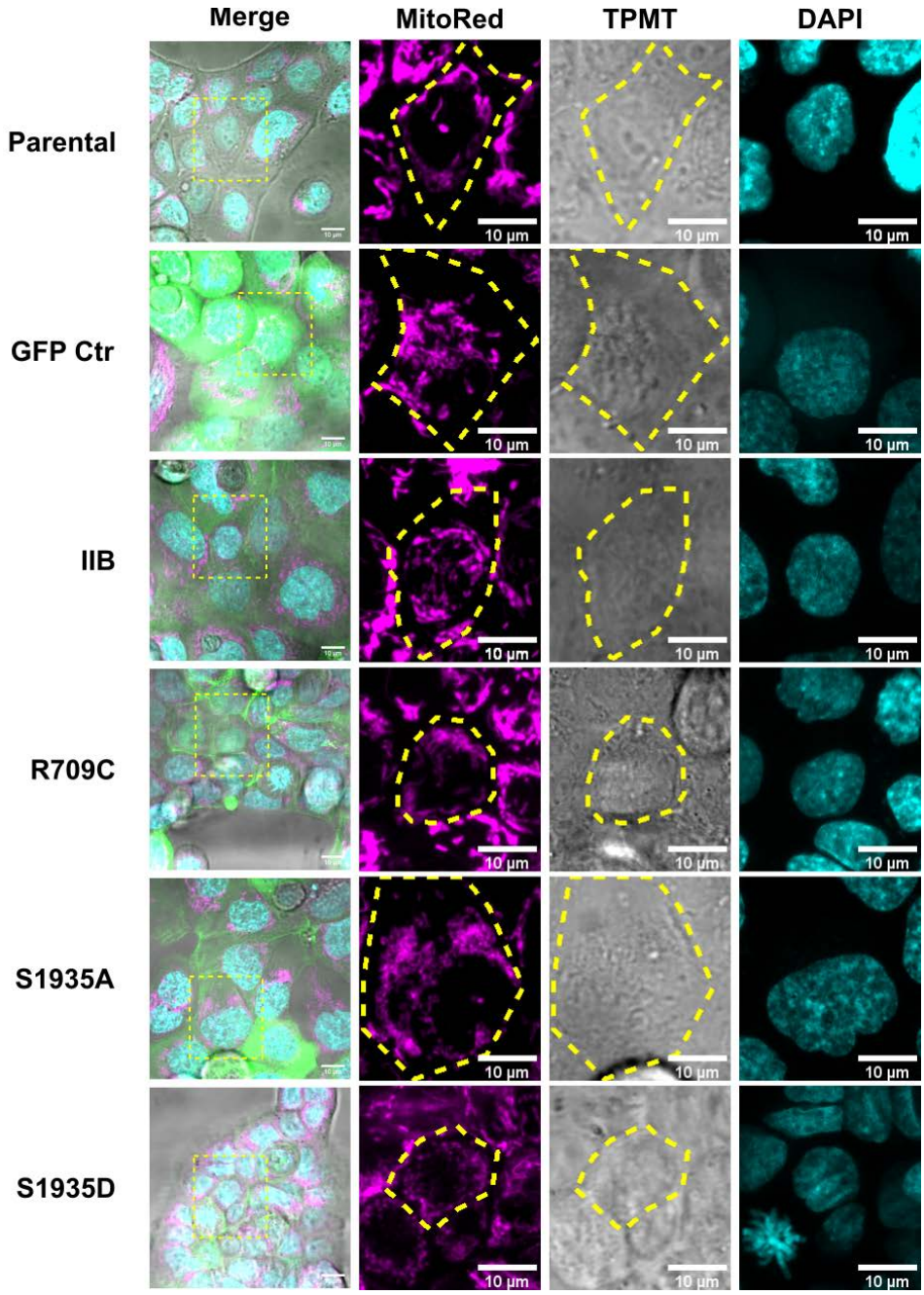

Sup. Fig. 3. Zoomed-in images of mitochondria in cells expressing NMII variants. Merged, MitoRed, transmission photomultiplier tube (tPMT), and DAPI images are provided. Parental cells and cells expressing GFP are provided as controls. Scale bars are 10 µm.

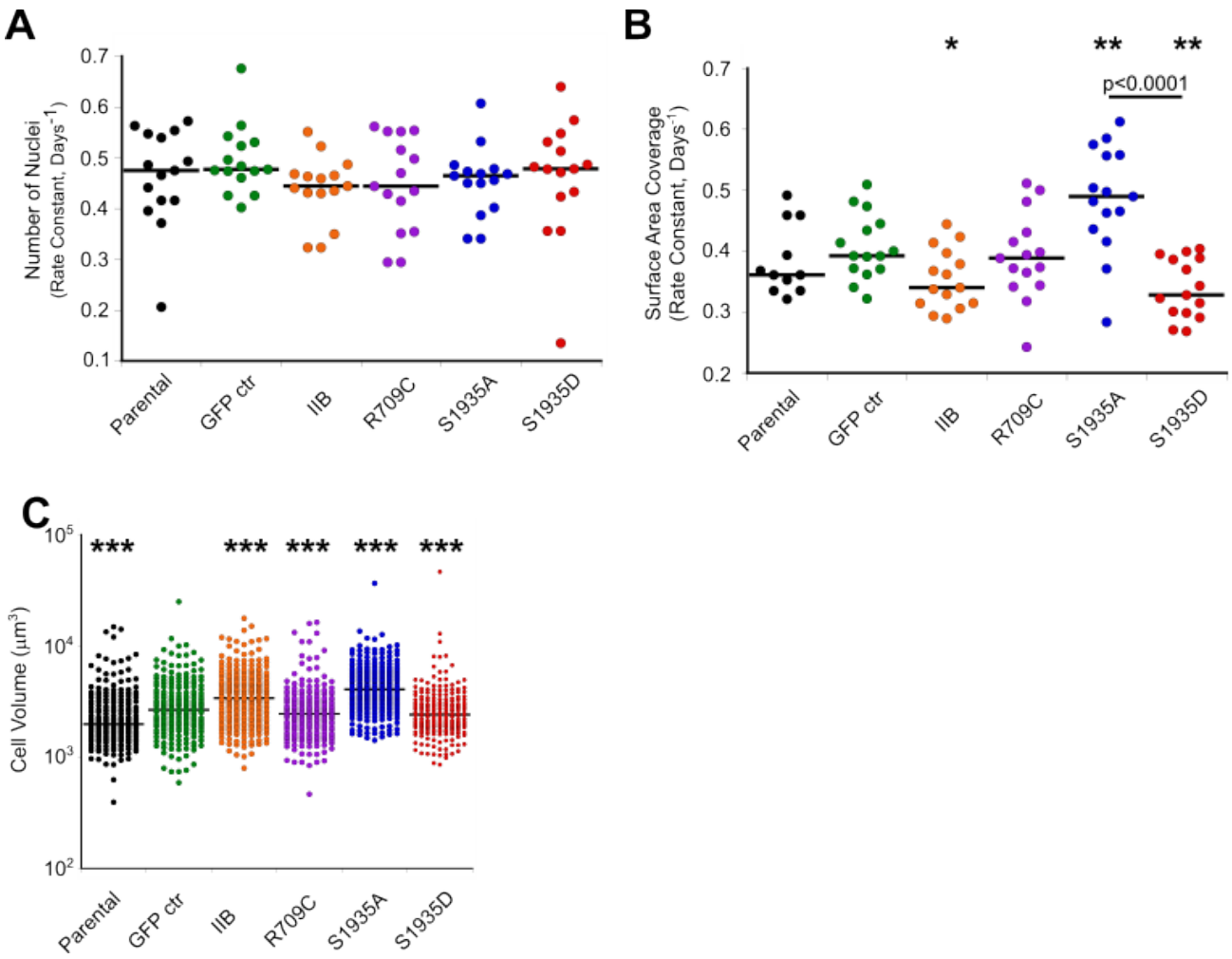

Sup. Fig. 4. Adaptation to exogenous NMIIB expression does not alter proliferation, but cell spreading and size. (A-B) Proliferation rates were determined by imaging and counting nuclei daily for 6 days after seeding Panc10.05 stable cells. Nuclei counts were then plotted over the time course using the median and standard deviation from the nine fields of view (FOV) taken per well per day. These data were then to an exponential curve and the rate constant from each experiment was plotted as a measure of proliferation rates (A). Data are pooled from four biological replicates done in technical triplicate or quadruplet (n=15). Outliers were not statistically considered with one-way ANOVA p=0.35866. **(B)** In the same experiments done in (A), bright field images were acquired to quantify the rate of surface area coverage by Panc10.05 stable cells. From these images, the percent of surface area covered by cells was quantified using the PHANTAST macro in fiji and plotted the median and standard deviation from nine FOVs per well per day. These data were then to an exponential curve and the rate constant from each experiment was plotted as a measure of rates of surface area coverage (B). Data are pooled from four biological replicates done in technical triplicate or quadruplet (n-15). Outliers were not statistically considered with one-way ANOVA p<0.0001, followed by Fisher's LSD *p<0.05, **p<0.005 compared to GFP ctr. **(C)** Cell volume was determined by trypsinizing Panc10.05 stable cells, allowing them to relax for 5 minutes, and then imaging 20 FOVs of rounded cells in suspension. Volume was determined by measuring the diameter of rounded cells and extrapolating volume (see methods). Data are pooled from two independent experiments. Outliers were not statistically considered with one-way ANOVA p<0.0001, followed by Fisher's LSD ***p<0.0001 compared to GFP ctr. Outliers are still represented in graphs and bars are medians.

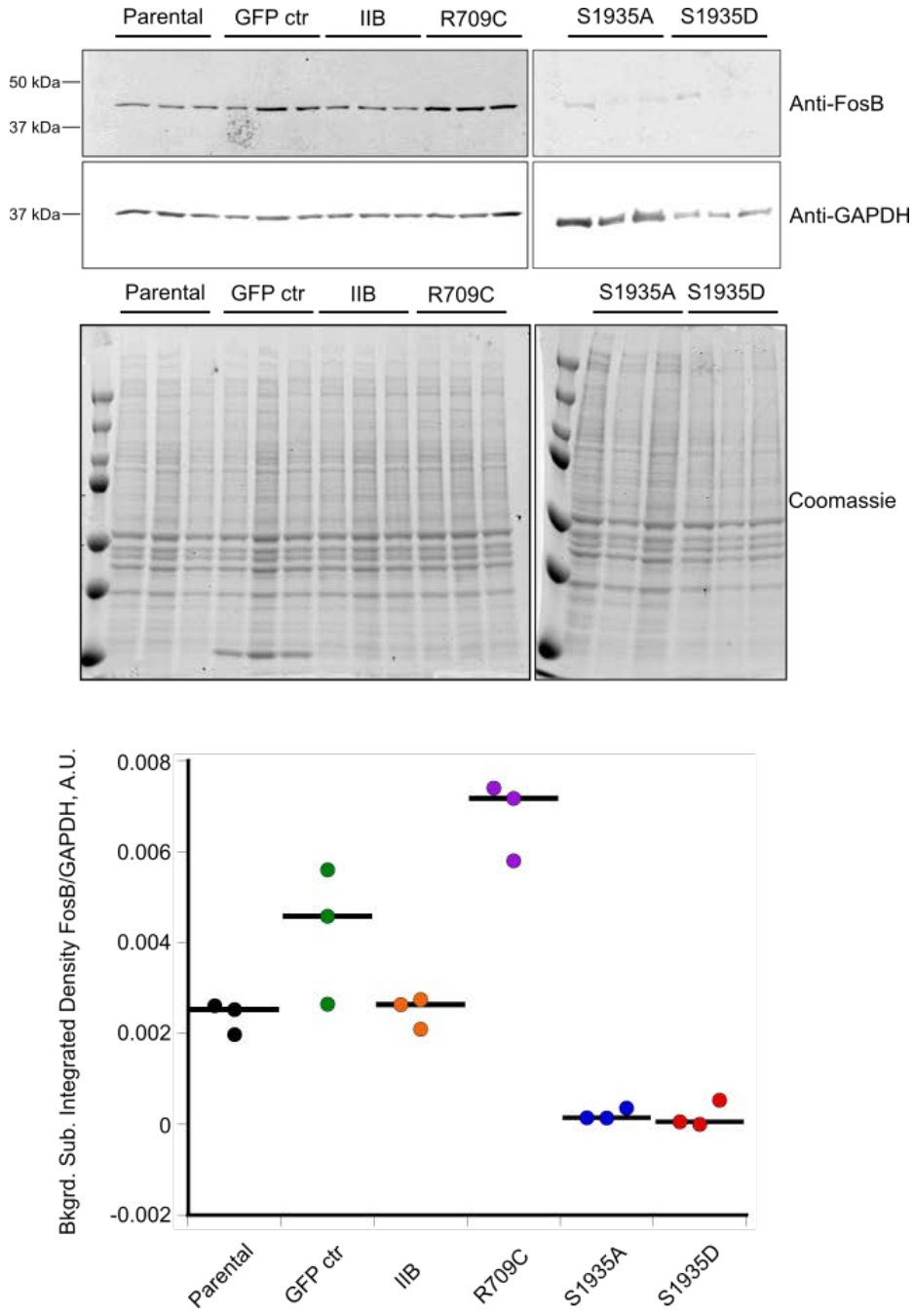

Sup. Fig. 5. FosB expression is reduced when NMIIB S1935A and S1935D are introduced. Top row, Western analysis is conducted to detect FosB expression. GAPDH is probed for a loading control. Middle row, Image of the Coomassie stained gel corresponding to the western blot in the top row. Bottom row, Quantification of the western by normalizing the integrated signal to the GAPDH signal after background subtraction.

Supplemental Table 1. Antibody and Oligonucleotides used in this study.

Antibodies					
Target	**Ig Type**	**Assay**	**Dilution**	**Source**	**Cat. #**
NMIIA	rabbit	Cyto. Frac.	1:500	BioLegend	909801
NMIIB	mouse	Cyto. Frac.	1:500	Developmental Studies Hybridoma Bank	CM11-23
NMIIC	rabbit	Cyto. Frac.	1:500	Cell Signaling	8189
GFP	mouse	Westerns	1:1000	ThermoFisher	MA5-15256
GAPDH	mouse	Westerns	1:1000	Proteintech	60004-Ig
GAPDH	rabbit	Westerns	1:1000	Cell Signaling	51745
FOSB	rabbit	Westerns	1:10000	Abcam	ab184938

Oligonucleotides	
Name	**Sequence**
PK10	CATGGTCCTGCTGGAGTTCGTG
PK12	TCTGGACTCTTCTGTGTAGTTATA
PK13	TGATGTAACTGGCTATATCGTTGGGGCC
ABF4	GGCCCTTTTGGATGAAGAAT
ABF5	TCCAAATGCTATTCCTAAAGGTT
ABF6	GAAACCAAATCCTCCAAAATGA
ABF7	AAGGCCGAAAAGCAGAAAAG
ABF8	GGAGAAGAACAGTCTTCAGG
ABF10	GTCTGGAAGCTCGGATCG
ABF12	GGAGCTGGAAGACGAACTCC
ABR3	CCGCTCCAGTTGCTGGCGTGC

Table S12. Summary of Phenotypes vs. Strain/NMIIB Variant.

NMIIB Variant	Fraction Cytoskeletal		Mechanical Impact		Metabolism Properties				Mitochondria per unit area	Cell size
	Increased Assembly of NMIIB	Increased Assembly of Other NMIIs	Cortical Tension	Mechano-response	ATP Production	Basal OxPhos ATP Production	Spare Respiratory Capacity	Decreased Glycolytic Dependence		
NMIIB		+	decreased	yes			decreased			
R709C	+	+		no	decreased		decreased	yes	increased	
1935A		+	decreased	no		increased	decreased		increased	larger
1935D	+	+		yes	decreased		decreased	yes	increased	smaller

Table S13. Endogenous NMII expression is not increased by exogenous NMIIB expression.

	Parental	GFP ctr	NMIIB	R709C	1935A	1935D
GAPDH (mean fpkm)	992.2833	1069.025	986.1216	1021.968	1569.686	1104.562
GAPDH Norm. to Parental	1	1.077339	0.99379	1.029915	1.581893	1.113151
NMIIB (mean fpkm)	1.065308	1.061795	71.14466	72.28625	429.6488	57.87301
NMIIB Norm. to Parental	1	0.996702	66.78316	67.85476	403.3093	54.32513
NMIIA (mean fpkm)	111.8046	103.6019	137.8626	113.4047	107.8968	118.6735
NMIIA Norm. to Parental	1	0.926634	1.233067	1.014312	0.965048	1.061436
NMIIC (mean fpkm)	11.11338	9.731321	8.869329	9.300411	3.340595	8.879381
NMIIC Norm. to Parental	1	0.87564	0.798077	0.836866	0.300592	0.798981

Mean fragments per kilobase million (fpkm) counts and as well as fpkm reads normalized to the parental control are shown from triplicates used in RNAseq study.